

Variational Methods in Image Matching and Motion Extraction in Level set and PDE Based Reconstruction Methods: Applications to Inverse Problems and Image Processing

Martin Rumpf*

Abstract. In this chapter we are concerned with variational methods in image analysis. Special attention is paid on free discontinuity approaches of Mumford Shah type and their application in segmentation, matching and motion analysis. We study combined approaches, where one simultaneously relaxes a functional with respect to multiple unknowns. Examples are the simultaneously extraction of edges in two different images for joint image segmentation and image registration or the joint estimation of motion, moving object, and object intensity map. In these approaches the identification of one of the unknowns improves the capability to extract the other as well. Hence, combined methods turn out to be very powerful approaches. Indeed, fundamental tasks in image processing are highly interdependent: Registration of image morphology significantly benefits from previous denoising and structure segmentation. On the other hand, combined information of different image modalities makes shape segmentation significantly more robust. Furthermore, robustness in motion extraction of shapes can be significantly enhanced via a coupling with the detection of edge surfaces in space time and a corresponding feature sensitive space time smoothing.

Furthermore, one of the key tools throughout most of the methods to be presented is nonlinear elasticity based on hyperelastic and polyconvex energy functional. Based on first principles from continuum mechanics this allows a flexible description of shape correspondences and in many cases enables to establish existence results and one-to-one mapping properties.

Numerical experiments underline the robustness of the presented methods and show applications on medical images and biological experimental data.

This chapter is based on a couple of recent articles [8,49,29,30,63] published by the author together with Leah Bar, Benjamin Berkels, Marc Droske, Nathan Litke, Guillermo Sapiro, and Benedikt Wirth.

*Bonn University, email: martin.rumpf@ins.uni-bonn.de

1 Some prerequisites

In this section, we will introduce basic notion used throughout the chapter and consider the general methodology for finite element type discretization of variational free discontinuity problems.

1.1 Image Morphology

We are going to review different notions of image morphology and develop here a new one that is in particular appropriate for the use in variational approaches where images or shapes are linked to each other by nonlinear deformations.

In mathematical terms, two images $u, v : \Omega \rightarrow \mathbb{R}$ with $\Omega \subset \mathbb{R}^d$ for $d = 2, 3$ are called morphologically equivalent, if they only differ by a change of contrast, i. e., if $u(x) = (\beta \circ v)(x)$ for all $x \in \Omega$ and for some function $\beta : \mathbb{R} \rightarrow \mathbb{R}$ [1,64]. Here, one usually restricts to contrast changes $\beta : \mathbb{R} \rightarrow \mathbb{R}$, which are strictly monotone and continuous functions. Obviously, such a contrast modulation does not change the order and the shape of level sets. Due to the enforced monotonicity, the same holds for the super level sets $l_c^+[u] = \{x : u(x) \geq c\}$. Thus, a usual description of the morphology $\mathcal{M}[u]$ of an image u is given by the upper topographic map, defined as the set of all these sets

$$\mathcal{M}[u] := \{l_c^+[u] : c \in \mathbb{R}\}.$$

Unfortunately, this set based definition is not feasible for the variational approach we intend to discuss. Furthermore, the restriction to monotone contrast changes conflicts with medical applications and medical morphology. In what follows, we derive an alternative notion based on a regular and a singular morphology. It can directly be used in variational approaches and allows us to get rid of the monotonicity assumption if appropriate. Let us suppose the image function $u : \Omega \rightarrow \mathbb{R}$ on an image domain $\Omega \subset \mathbb{R}^d$ to be in SBV [4]. Hence, we consider functions $u \in L^1(\Omega)$ of which the derivative $\mathcal{D}u$ is a vector-valued Radon measure with vanishing Cantor part. In fact, at edges we allow for jumps and thus infinitely steep gradients concentrated on a sufficiently regular, lower dimensional set, but not for jumps on sets of fractal dimensions. We consider the usual splitting $\mathcal{D}u = \mathcal{D}^{ac}u + \mathcal{D}^s u$ [4], where $\mathcal{D}^{ac}u$ is the regular part, which is the usual image gradient apart from edges and absolutely continuous with respect to the Lebesgue measure \mathcal{L} on $\Omega \subset \mathbb{R}^d$, and a singular part $\mathcal{D}^s u$, which represents the jump and is defined on the edge set \mathcal{S} , which consists of the edges of an image. We denote by n^s the vector valued measure representing the normal field on \mathcal{S} , such that the representation $\mathcal{D}^s u = (u^+ - u^-)n^s$ holds for the singular part of the derivative. Here u^+ and u^- are the upper and the lower (approximate limsup and liminf [4]) values at the edge \mathcal{S} , respectively. This normal field is defined \mathcal{H}^{d-1} a.e. on \mathcal{S} . Obviously, n^s is a morphological invariant as long as we consider continuous strictly monotone contrast modulating functions β .

Now, we focus on the regular part of the derivative. First, we adopt the classical gradient notion $\nabla^{ac}u$ for the \mathcal{L} density of $\mathcal{D}^{ac}u$, i. e., $\mathcal{D}^{ac}u = \nabla^{ac}u \mathcal{L}$ [4]. As long as it is defined, the normalized gradient $\frac{\nabla^{ac}u(x)}{|\nabla^{ac}u(x)|}$ is the outer normal on the upper topographic set $l_{u(x)}^+[u]$ and thus again a morphological quantity. It is undefined on the flat image

region $F[u] := \{x \in \Omega : \nabla^{ac} u(x) = 0\}$. We introduce n^{ac} as the normalized regular part of the gradient

$$n^{ac} = \chi_{\Omega \setminus F[u]} \frac{\nabla^{ac} u}{|\nabla^{ac} u|}$$

with support $\Omega \setminus F$ and denote it the Gauss map of the image u . With the regular normal n^{ac} and the singular normal measure n^s at hand, we are now able to redefine the morphology $\mathcal{M}[u]$ of an image u as a vector valued Radon measure on Ω with

$$\mathcal{M}[u] = n^{ac} \mathcal{L} + n^s, \quad (1)$$

which is up to the flat set $F[u]$ of unit length. We call $n^{ac} \mathcal{L}$ the regular morphology and n^s the singular morphology. It turns out that this new notion is equivalent to the above definition on sufficiently regular image functions. It completely describes the topographical shape information of the image u . If we skip the orientation of the vectors n^{ac} and n^s in (1) and replace them by the corresponding line subspaces we are able to treat general, not only monotone, contrast changes. This is actually reflected by our algorithm.

1.2 The Mumford–Shah model in image analysis

At first, let us consider a fundamental image segmentation model, which will later pick up and combine with other techniques and integrate in joint variational approaches. In their pioneering paper, Mumford and Shah [56] proposed the minimization of the following energy functional:

$$\mathcal{E}_{MS}[u, \mathcal{S}_u] = \int_{\Omega} (u - u^0)^2 d\mathcal{L} + \mu \int_{\Omega \setminus \mathcal{S}_u} |\nabla u|^2 d\mathcal{L} + \eta \mathcal{H}^{d-1}(\mathcal{S}_u), \quad (2)$$

where u^0 is the initial image defined on an image domain $\Omega \subset \mathbb{R}^d$ and μ, η are positive weights. Here, one asks for a piecewise smooth representation u of u^0 and a singularity set \mathcal{S}_u consisting of the image edges, such that u approximates u^0 in a least-squares sense. The intensity function u ought to be smooth apart from the free discontinuity \mathcal{S}_u and in addition \mathcal{S}_u should be small with respect to the $d - 1$ -dimensional Hausdorff-measure [4]. Here, we will make use of this approach to regularize images in a suitable way prior to the matching and simultaneously to split image morphology into a regular part related to contour sets of the piecewise smooth portions of an image and a singular part consisting of the edge set. Even though the Mumford-Shah approach itself is not morphological (e.g. intensity scaling may lead to an identification of previously overlooked edges) prominent edges are expected to be uniformly identified basically independent of the image contrast. Mathematically, this Mumford-Shah problem has been treated in the space of functions of bounded variations BV , more precisely in the specific subset SBV [4]. A related, alternative decomposition has been proposed by Rudin, Osher and Fatemi [61]. They suggested to minimize $|u|_{BV} + \lambda |u - u^0|_{L^2}^2$ in BV .

The explicit treatment of the edge set \mathcal{S} is neither theoretically nor with respect to a numerical approximation very handsome. Hence let us review briefly the approximation

of the Mumford-Shah functional (2), proposed by Ambrosio and Tortorelli [3]. They describe the edge set \mathcal{S}_u by a phase field function v , which is supposed to be small on \mathcal{S}_u and close to 1 elsewhere. Phase field models are widespread in physics, where they represent a material order parameter and thus describe interfaces in solids or fluids. In fact, one asks for minimizers of the energy functional

$$\mathcal{E}_{AT}^\varepsilon[u, v] = \int_{\Omega} (u - u^0)^2 + \mu(v^2 + k_\varepsilon)|\nabla u|^2 + \eta \varepsilon |\nabla v|^2 + \frac{\eta}{4\varepsilon}(1 - v)^2 \, d\mathcal{L}, \quad (3)$$

where ε is a scaling parameter and $k_\varepsilon = o(\varepsilon)$ a small positive regularizing parameter. For larger ε one obtains coarse, blurred representations of the edge sets and corresponding smoother images u . For decreasing ε the representation of the edges is successively refined and more and more image details are included. We will make use of this inherent multi scale in cascadic minimization algorithms.

1.3 Finite Element approximation in imaging

To prepare the later discussion of discrete algorithms for a variety of different variational models, we will present in this section the discrete representation of images in finite element spaces and two different types of finite element discretizations for the classical Mumford and Shah segmentation model already reviewed above. Furthermore, we will introduce some useful multi scale treatment of image data.

We consider images as piecewise multilinear (bilinear in the case of 2D applications) finite element functions on a regular image domain. We denote the corresponding finite element space \mathcal{V}^h , where h represents the underlying grid size. For some applications it is more convenient to further subdivide the cells into simplices via a splitting of rectangles into 2 triangles and hexahedrons into 6 tetrahedrons. This straightforward subdivision set does not modify the underlying degrees of freedom. In fact, it only influences the numerical quadrature for the finite element assembly. Each pixel or voxel value corresponds to a node of the regular mesh and a set of nodal values uniquely identifies a finite element function in \mathcal{V}^h . We apply these finite element space not only for the representation of discrete images but also for the discretization of all other unknown appearing in the models, such as phase fields v or the components of vector valued quantities such as elastic deformations ϕ . Throughout this chapter continuous quantities are always denoted by lower case letters, whereas upper case letters are used for discrete functions. The corresponding nodal finite element vectors are marked with a bar on top, e.g. \bar{U} is considered to be the discrete counterpart of an image function u and \bar{U} denotes the corresponding nodal vector. Linear systems of equations, which arise from quadratic functionals are usually solved based on a preconditioned conjugate gradient method [41]. In the assembly of these linear systems we apply on each grid cell higher order Gaussian quadrature rule if the local integrand is not polynomial.

For the ease of implementation we suppose dyadic resolutions of the images with $2^L + 1$ pixels or voxels in each direction. Thus, we are able to build a hierarchy on grids with $2^l + 1$ nodes in each direction for $l = L, \dots, 0$. We restrict every finite element function via a straightforward nodal value evaluation to any of these coarse grid spaces. The construction of the multigrid hierarchy allows to solve coarse scale problems in our

multi scale approach on coarse grids. Indeed, scale k is resolved on the corresponding $l(k)$ th grid level (e.g. with $l(k) = k$). First of all, we apply this throughout all variational models to be discussed here in cascadic type energy minimization approaches. For this purpose, we start minimizing the underlying nonlinear functionals on a coarse scale and then successively refine the grid, prolongate the solution onto the next finer grid and take this as initial data for the further relaxation of the corresponding discrete functional. Furthermore, the grid hierarchy is used in regularized gradient descent schemes. The regularization is based on a smoothing metric in the definition of the gradient. Effectively, we consider an H^1 -type metric where the smoothing is performed via multigrid V cycles corresponding to a standard finite element implementation of the differential operator $\mathbb{1} - \frac{\sigma^2}{2} \Delta$. For details we refer to [21,29].

At various places, we have to evaluate discrete functions U at pushed forward or pulled back positions under a discrete deformation Φ . In both cases, we replace the exact evaluation of these functions by a simple and effective interpolation. Indeed, we replace $U \circ \Phi$ by $\mathcal{I}(U \circ \Phi)$, where \mathcal{I} is the classical Lagrangian interpolation on the grid nodes. Thus, each grid node is mapped under the deformation Φ onto the image domain, U is evaluated at these positions, and these values define our new finite element function. Analogously, $U \circ \Phi^{-1}$ is replaced by $\mathcal{I}(U \circ (\mathcal{I} \circ \Phi)^{-1})$. Here, we proceed as follows. We map each grid cell under the deformation onto the image domain. Next we identify all grid nodes, which are located on this deformed cell. These grid nodes are then mapped back under the inverse local deformation. Now, interpolation is applied to retrieve requested values of the finite element function U . Inversion of multilinear deformation would lead to nonlinear equations. To avoid this shortcoming, we cut each cell as mentioned above virtually into simplices. On these simplices, affine functions approximate in a straightforward way the multilinear functions. Thus, we replace the regular cells in the retrieval algorithm by the simplices and end up with piecewise affine inverse mappings.

In the next two paragraphs we will describe two significantly different approaches to discretize the Mumford Shah functional. The first is based on a direct implementation of the approach and uses a level set description of the edge set, whereas the other implements the Ambrosio Tortorelli approximation in a straightforward way.

Composite finite elements for level set described edge contours In what follows, we will investigate an energy descent method directly for the Mumford Shah functional. The Mumford Shah functional can be regarded as a shape optimization problem. For given edge contour \mathcal{S} , the image intensity $u = u[\mathcal{S}]$ solves a quadratic variational problem. Thus, we rewrite the Mumford Shah functional as a shape functional $\hat{\mathcal{E}}[\mathcal{S}] := \mathcal{E}_{\text{MS}}[u[\mathcal{S}], \mathcal{S}]$ depending solely on the edge contour \mathcal{S} . Hence, the shape gradient of the functional with respect to variations in \mathcal{S} incorporates quantities based on $u[\mathcal{S}]$. Here, we make use of the nowadays already classical shape sensitivity calculus. For details we refer to the books of SOKOŁOWSKI & ZOLÉSIO [66] or DELFOUR & ZOLÉSIO [27]. Furthermore, the Appendix of [42] gives a nice overview. Smooth variations of the edge contour \mathcal{S} can be expressed via normal variations $x + t \vartheta n[\mathcal{S}]$ of points x on \mathcal{S} in normal direction for small $t \in \mathbb{R}$ and a function θ on \mathcal{S} . Here, $n[\mathcal{S}]$ denotes the normal on \mathcal{S} , which coincides with the density of n^s introduced in Section 1.1. Let

we denote by $S(t)$ the resulting family of edge contours. The shape derivative of $\hat{\mathcal{E}}[S]$ is then defined as

$$\partial_S \hat{\mathcal{E}}[S](\vartheta) = \frac{d}{dt} \mathcal{E}[S(t)]|_{t=0}.$$

For a given smooth function $g : \Omega \rightarrow \mathbb{R}$, the derivative of functional $\int_S g d\mathcal{H}^{d-1}$ is given by $\int_S (\partial_{n[S]} g + gh) \vartheta d\mathcal{H}^{d-1}$, where h is the mean curvature in S . Given a function $f : \Omega \rightarrow \mathbb{R}$ which might jump on S , the shape derivative of the functional $\int_\Omega f d\mathcal{L}$ is given by $\int_S \llbracket f \rrbracket \vartheta d\mathcal{H}^{d-1}$, where $\llbracket f \rrbracket = \lim_{\varepsilon \rightarrow 0} (f(x + \varepsilon n[S]) - f(x - \varepsilon n[S]))$ denotes the jump of f on S . With these tools available, we obtain for the shape derivative of the Mumford Shah shape functional

$$\partial_S \hat{\mathcal{E}}[S](\vartheta) = \int_S \left(\eta h + \llbracket |u[S] - u^0|^2 + \mu |\nabla u[S]|^2 \rrbracket \right) \vartheta d\mathcal{H}^{d-1}. \quad (4)$$

Furthermore, the minimizer $u = u[S]$ of the Mumford Shah functional for fixed S solves the corresponding Euler Lagrange equations, which is given by the linear elliptic PDE $\mu \Delta u + (u - u^0) = 0$ on $\Omega \setminus S$ and the boundary conditions $\partial_{n[S]} u^+ = 0$ and $\partial_{n[S]} u^- = 0$ where u^\pm indicate the possibly discontinuous function on both sides of S separately.

Now, let us briefly describe how to discretize this shape derivative in a proper way. We suppose that the edge contour can be described as the zero set $[\xi = 0]$ of a level set function ξ . Hence, S is in particular assumed to be closed relative in Ω . Let us denote by $\mathcal{E} \in \mathcal{V}^h$ a finite element approximation of this interface. Here, we restrict to simplicial finite elements on the above already introduced subdivision of rectangular grids into triangulations. The now discrete shape $S = [\mathcal{E} = 0]$ separates the domain into two polygonal regions $\Omega^+[\mathcal{E}] = [\mathcal{E} > 0]$ and $\Omega^-[\mathcal{E}] = [\mathcal{E} < 0]$. For fixed \mathcal{E} we introduce two new finite element space $\mathcal{V}_+^h[\mathcal{E}]$ and $\mathcal{V}_-^h[\mathcal{E}]$ adapted to the two domains $\Omega^+[\mathcal{E}]$ and $\Omega^-[\mathcal{E}]$. In fact, for every finite element basis function Θ^i whose support intersects $\Omega^\pm[\mathcal{E}]$, we define the composite finite element basis function $\Theta_i^\pm = \chi_{\Omega^\pm[\mathcal{E}]} \Theta_i$ [40,39].

The span of all these basis function form the composite finite element spaces $\mathcal{V}_+^h[\mathcal{E}]$ and $\mathcal{V}_-^h[\mathcal{E}]$, respectively. Now, we consider discrete finite element counterparts U^+ and U^- of $u[S]$ on $\Omega^+[\mathcal{E}]$ and on $\Omega^-[\mathcal{E}]$, separately. Indeed, define $U^\pm \in \mathcal{V}_\pm^h[\mathcal{E}]$ as the solution of

$$0 = \int_{\Omega^\pm[\mathcal{E}]} \mu \nabla U^\pm \cdot \nabla \Theta + (U^\pm + \mathcal{I}_h^\pm u^0) \Theta d\mathcal{L}$$

for all functions $\Theta \in \mathcal{V}_\pm^h[\mathcal{E}]$, where \mathcal{I}_h^\pm denotes a piecewise constant interpolation based on simplicial mid point evaluation. In matrix vector notation, we obtain a system of linear equations for each nodal vectors \bar{U}^\pm of the finite element functions $U^\pm = U^\pm[\mathcal{E}]$:

$$(\mu \mathbf{L}^\pm[\mathcal{E}] + \mathbf{M}^\pm[\mathcal{E}]) \bar{U}^\pm = \mathbf{M}^\pm[\mathcal{E}] \overline{\mathcal{I}_h^\pm u^0}$$

The coefficients in the matrix and of the right hand side depend on the shape $S[\mathcal{E}]$ described by the current level set function \mathcal{E} , i. e. $\mathbf{L}^\pm[\mathcal{E}] = \left(\int_{\Omega^\pm[\mathcal{E}]} \nabla \Theta_j \cdot \nabla \Theta_i d\mathcal{L} \right)_{ij}$ and $\mathbf{M}[\mathcal{E}] = \left(\int_{\Omega^\pm[\mathcal{E}]} \Theta_j \Theta_i d\mathcal{L} \right)_{ij}$ are the composite finite element stiffness and mass matrix,

respectively. Here, the indices i and j are running over all active indices in \mathcal{V}_\pm^h .

The shape variation $\partial_S \hat{\mathcal{E}}[\mathcal{S}]$ has a singular density concentrated on the edge set. Thus, we consider a shape gradient $\text{grad}_S \mathcal{E}[\mathcal{S}]$ based on a regularizing metric. Let us recall that a gradient always depends on an underlying metric and is defined as the representation of the variation in this metric. In our case we use the H^1 scalar product $(v, w)_\sigma = \int_\Omega \frac{\sigma^2}{2} \nabla u \cdot \nabla v + uv \, d\mathcal{L}$ for some constant $\sigma > 0$ and define

$$(\text{grad}_S \hat{\mathcal{E}}[\mathcal{S}], \theta)_\sigma = \partial_S \hat{\mathcal{E}}[\mathcal{S}](\theta)$$

for all smooth test functions θ on Ω . The discrete counter part $\text{grad}_{\mathcal{S}[\mathcal{E}]} \mathcal{E}[\mathcal{S}[\mathcal{E}]]$ is the finite element function in \mathcal{V}^h such that

$$\begin{aligned} (\text{grad}_S \mathcal{E}[\mathcal{S}[\mathcal{E}]], \Theta)_\sigma &= \partial_S \mathcal{E}[\mathcal{S}[\mathcal{E}]](\Theta) \\ &= \int_{\mathcal{S}[\mathcal{E}]} (\eta H + [|U[\mathcal{S}[\mathcal{E}]] - u^0|^2 + \mu |\nabla U[\mathcal{S}[\mathcal{E}]]|^2]) \Theta \, d\mathcal{H}^{d-1} \end{aligned} \quad (5)$$

for all test functions $\Theta \in \mathcal{V}^h$ and a suitable discrete mean curvature H on $\mathcal{S}[\mathcal{E}]$. Each evaluation of $\text{grad}_S \mathcal{E}[\mathcal{S}[\mathcal{E}]]$ requires the solution of linear system of equations. The resulting regularized discrete gradient can now be used in a standard level set approach. Indeed, the level set equation $\partial_t \xi + |\nabla \xi| v = 0$ identifies normal variations v of level sets $[\xi = c]$ with variations $s = \partial_t \xi$ of the level set function. Hence, $-|\nabla \xi|^{-1} \text{grad}_{\mathcal{S}[\xi]} \mathcal{E}[\mathcal{S}[\xi]]$ is the corresponding descent direction of the functional $\xi \rightarrow \mathcal{E}[\mathcal{S}[\xi]]$ in the spatially still continuous case. The discretization based on standard finite elements is straightforward and thus omitted here.

Finally, we have all ingredients at hand to derive an algorithm for the minimization of the discrete Mumford Shah functional. In each step of the algorithm we first compute for a given discrete level set function \mathcal{E} the discrete image intensities $U^+[\mathcal{E}]$ and $U^-[\mathcal{E}]$. Then, we can evaluate the right hand side in (5) and thus compute the discrete shape gradient $\text{grad}_S \mathcal{E}[\mathcal{S}[\mathcal{E}]] \in \mathcal{V}^h$. From this, we deduce the discrete descent direction of the level set shape functional. Finally, a step sized controlled 1D descent strategy is applied. For details on this approach and a comparison to alternative approaches in the context of image segmentation and registration we refer to [28,31].

Finite elements for the phase field model Now, let us present an algorithmic alternative to the previously described discrete sharp interface model. We pick up the phase field approach (3) by Ambrosio and Tortorelli [3] and rephrase it for discrete image intensities and phase fields in the standard finite element space \mathcal{V}^h . Hence, we ask for discrete minimizers of the energy

$$\mathcal{E}_\varepsilon[U, V] = \int_\Omega \left\{ (U - \mathcal{I}_h u^0)^2 + \mu (V^2 + k_\varepsilon) |\nabla U|^2 \right\} + \eta \left(\varepsilon |\nabla V|^2 + \frac{(1-V)^2}{4\varepsilon} \right) \, d\mathcal{L}$$

over all $U, V \in \mathcal{V}^h$. Here, \mathcal{I}_h denotes the piecewise linear Lagrangian interpolation. The corresponding Euler Lagrange equations are

$$0 = \int_\Omega (U - \mathcal{I}_h u^0) \Theta + \mu (V^2 + k_\varepsilon) \nabla U \cdot \nabla \Theta \, d\mathcal{L}, \quad (6)$$

$$0 = \int_\Omega \mu V \Xi |\nabla U|^2 + \eta \int_\Omega \left(\varepsilon \nabla V \cdot \nabla \Xi + \frac{(V-1)}{4\varepsilon} \Xi \right) \, d\mathcal{L} \quad (7)$$

for all $\Theta, \varepsilon \in \mathcal{V}^h$. The underlying mesh is supposed to consist of simplices. Hence, the different terms in the integrant are at most quadratic and can be integrated exactly using appropriate quadrature rules. The equation (6) is linear in U and the equation (7) is linear in V . In matrix vector notation, we obtain two systems of linear equations for the nodal vectors \bar{U} and \bar{V} which represent the finite element functions U and V , respectively:

$$\begin{aligned} (\mu \mathbf{L}[V^2 + k_\varepsilon] + \mathbf{M}[1]) \bar{U} &= \mathbf{M}[1] \overline{\mathcal{I}_h u^0} \\ \left(\eta \varepsilon \mathbf{L}[1] + \mathbf{M}[\mu |\nabla U|^2 + \frac{\eta}{4\varepsilon}] \right) \bar{V} &= \frac{\eta}{4\varepsilon} \mathbf{M}[1] \bar{1} \end{aligned}$$

The coefficients in the matrix and of the right hand side depend on the corresponding other discrete variable. Here $\mathbf{L}[\omega] = (\int_\Omega \omega \nabla \Theta_j \cdot \nabla \Theta_i d\mathcal{L})_{ij}$ and $\mathbf{M}[\omega] = (\int_\Omega \omega \Theta_j \Theta_i d\mathcal{L})_{ij}$ are the weighted stiffness and mass matrix, respectively. The weight is denoted by ω and Θ_i are the hat basis functions indexed by the nodal index i , $\overline{\mathcal{I}_h u^0}$ is the nodal vector corresponding to $\mathcal{I}_h u^0$, and $\bar{1}$ is the vector with components all equal to 1. In [10] Bourdin has shown the Γ -convergence of the discretized functionals to the corresponding continuous one. The actual algorithm now consists of an alternating minimization, which is given in pseudo code notation by the following code fragment:

```

DiscreteAT {
   $k = 0$ ; initialize  $\bar{U}^0 = \overline{\mathcal{I}_h u^0}$  and  $\bar{V}^0 \equiv \bar{1}$ ;
  do {
    Solve  $(\mu \mathbf{L}[(V^k)^2 + k_\varepsilon] + \mathbf{M}[1]) \bar{U}^{k+1} = \mathbf{M}[1] \overline{\mathcal{I}_h u^0}$  for  $\bar{U}^{k+1}$ ;
    Solve  $(\eta \varepsilon \mathbf{L}[1] + \mu \mathbf{M}[|\nabla U^{k+1}|^2 + \frac{\eta}{\varepsilon}]) \bar{V}^{k+1} = \frac{\eta}{4\varepsilon} \mathbf{M}[1] \bar{1}$  for  $\bar{U}^{k+1}$ ;
     $k=k+1$ ;
  } while  $(|\bar{U}^k - \bar{U}^{k-1}| + |\bar{V}^k - \bar{V}^{k-1}| \geq \text{Threshold})$ 
}

```

Later, we will pick up this alternating minimization strategy in combination with a gradient descent scheme for additional quantities, primarily deformations, in joint segmentation and matching approaches.

1.4 Nonlinear elastic deformations

The correlation or matching of images or shapes requires a mathematical description in terms of a deformation which registers image or shape structures. These matching problems are known usually to be ill posed problems. Hence, in a variational setting a suitable regularization energy has to be considered. Here, we propose to use hyperelastic energy functionals $\mathcal{E}_{elast}[\phi]$ on deformations ϕ . In what follows we will motivate this type of regularization energy both from a physical and from a mathematical perspective.

A physical argument in favor of the hyperelastic model The regularization energy on deformations is based on classical concepts from continuum mechanics and in particular from the theory of elasticity. We give an exposition of the concept in three dimensions, the two dimensional case follows by analogy. For details we refer to the comprehensive

introductions in the books by Ciarlet or Marsden and Hughes [19,50]. Let Ω be an isotropic elastic body. We suppose $\psi = \mathbb{1}$ to represent the stress free deformation. Let us consider the deformation of length, area and volume under a deformation ϕ . Here we denote by \mathcal{H}^k the k -dimensional Hausdorff measure, i.e. $\mathcal{H}^d = \mathcal{L}$. We observe that the length of a curve $\gamma : [0, 1] \rightarrow \Omega$ undergoing the deformation ϕ is transformed via

$$\mathcal{H}^1(\phi(\gamma)) = \int_0^1 \left| \frac{\mathcal{D}\phi \circ \gamma}{dt} \right| d\mathcal{H}^1 = \int_0^1 \sqrt{\mathcal{D}\phi^T \mathcal{D}\phi \dot{\gamma} \cdot \dot{\gamma}} d\mathcal{H}^1.$$

Hence, $\mathcal{D}\phi^T \mathcal{D}\phi$ controls the change of length under the deformation, and in case of isotropic elasticity we confine with the norm $|\mathcal{D}\phi|_2$ as the term controlling the change of length, where $|A|_2 := \text{tr}(A^T A) = \sum_{i,j} A_{i,j} A_{i,j}$ for $A \in \mathbb{R}^{d,d}$. Secondly, the local volume transformation under a deformation ϕ is obviously controlled by $\det \mathcal{D}\phi$, i.e.

$$\mathcal{H}^d(\phi(V)) = \int_V |\det \mathcal{D}\phi(x)| d\mathcal{L}$$

for a volume $V \subset \Omega$. If $\det \mathcal{D}\phi < 0$, self penetration may be observed. Finally, let us consider the transformation of area elements. Let \mathcal{S} be a hypersurface patch with normal n and $T_x \mathcal{S}$ the tangent space of \mathcal{S} at a point x on \mathcal{S} . Suppose n^ϕ is the deformed normal on $T_x \phi[\mathcal{S}]$ at position $\phi(x)$. Hence, from $n^\phi \cdot \mathcal{D}\phi v = 0$ for all $v \in T_x \phi[\mathcal{S}]$ we derive

$$n^\phi = \frac{\text{cof} \mathcal{D}\phi n}{|\text{cof} \mathcal{D}\phi n|}$$

where $\text{cof} A = \det A A^{-T}$ for $A \in \mathbb{R}^{d,d}$. Thus the deformed area element is given by $\frac{\det \mathcal{D}\phi}{n^\phi \cdot \mathcal{D}\phi n}$ and we obtain

$$\begin{aligned} \mathcal{H}^{d-1}(\phi[\mathcal{S}]) &= \int_{\phi[\mathcal{S}]} d\mathcal{H}^{d-1} = \int_{\mathcal{S}} \frac{|\det \mathcal{D}\phi|}{|n^\phi \cdot \mathcal{D}\phi n|} d\mathcal{H}^{d-1} \\ &= \int_{\mathcal{S}} \frac{|\det \mathcal{D}\phi| |\mathcal{D}\phi^{-T} n|}{|\mathcal{D}\phi^{-T} n \cdot \mathcal{D}\phi n|} d\mathcal{H}^{d-1} = \int_{\mathcal{S}} |\det \mathcal{D}\phi \mathcal{D}\phi^{-T} n| d\mathcal{H}^{d-1} \\ &= \int_{\mathcal{S}} |\text{cof} \mathcal{D}\phi n| d\mathcal{H}^{d-1}. \end{aligned}$$

In analogy to the case of length control, $|\text{cof} \mathcal{D}\phi|_2 = \text{tr}(\text{cof} \mathcal{D}\phi^T \text{cof} \mathcal{D}\phi)$ is the proper measure for the change of area in an isotropic elastic body.

Based on these considerations we can define a simple physically reasonable isotropic elastic energy for $d = 3$, which separately cares about length, area and volume deformation and especially penalizes volume shrinkage:

$$\mathcal{E}_{elast}[\phi] := \int_{\Omega} W(|\mathcal{D}\phi|^2, |\text{cof} \mathcal{D}\phi|^2, \det \mathcal{D}\phi) d\mathcal{L} \quad (8)$$

where $W : \mathbb{R} \times \mathbb{R} \times \mathbb{R} \rightarrow \mathbb{R}$ is supposed to be convex. In particular, we will consider

$$W(I_1, I_2, I_3) := \alpha_1 |\mathcal{D}\phi|^{\frac{p}{2}} + \alpha_2 |\text{cof } \mathcal{D}\phi|^{\frac{q}{2}} + \alpha_3 \Gamma(\det \mathcal{D}\phi) \, d\mathcal{L} \quad (9)$$

with $\Gamma(D) = D^r + \frac{s}{r} D^{-s}$, $r, s > 0$ and $\alpha_1, \alpha_2, \alpha_3 > 0$. In nonlinear elasticity such materials laws have been proposed by Ogden [57], and for $p = q = 2$ we obtain the Mooney-Rivlin model [19]. More general, we can consider a so called polyconvex energy functional [25]. Hence, W and thereby $\mathcal{E}_{\text{elast}}[\phi]$ penalize volume shrinkage, i.e. $W(I_1, I_2, I_3) \xrightarrow{I_3 \rightarrow 0} \infty$ as reflected by the property of Γ above. The arguments of W are in fact the principle invariants of the matrix Jacobian of the deformation ϕ . It is worth to underline, that under these assumptions the function $\hat{W} : \mathbb{R}^{d,d} \rightarrow \mathbb{R}$ with

$$\hat{W}(A) := W(|A|^2, |\text{cof } A|^2, \det A)$$

is not convex [19]. Physically,

$$\sigma[\phi] = (\sigma_{ij}[\phi])_{i,j=1,\dots,d} := (\mathcal{D}_{A_{ij}} \hat{W}(\mathcal{D}\phi))_{i,j=1,\dots,d}$$

plays the role of the elastic Piola–Kirchhoff stress tensor. The built-in penalization of volume shrinkage, i. e. $\bar{W}(I_1, I_2, I_3) \xrightarrow{I_3 \rightarrow 0} \infty$, enables us to control local injectivity (cf. [5] and the next paragraph). Furthermore, a deformation which is locally isometric, i. e. $\nabla \phi_i^T(x) \nabla \phi_i(x) = \mathbb{1}$, is a local minimizer of the energy.

The physical advantages of the nonlinear elastic model are the following:

- It allows to incorporate large deformations with strong material and geometric nonlinearities, which cannot be treated by a linear approach.
- The dependency of the energy density \hat{W} follows from first principle and measures the physical effects of length, area, and volume distortion, which reflect the local distance from an isometry.
- Finally, it balances in an intrinsic way expansion and collapse of the elastic objects and hence frees us to impose artificial conditions on the expected image shape.

A mathematical argument in favor of the hyperelastic model The matching of 2D and 3D images - also known as image registration - is one of the fundamental tasks in image processing. Here, as we will see below, even for one of simplest possible matching energies standard regularization techniques fail, and the problem turns out not to be wellposed. With the help of a hyperelastic and polyconvex regularization we will be able to establish existence results.

One aims to correlate two images - a reference image u_R and a template image u_T - via an energy relaxation over a set of in general non rigid spatial deformations. Let us denote the reference image by $u_R : \Omega \rightarrow \mathbb{R}$ and the template image by $u_T : \Omega \rightarrow \mathbb{R}$. Both images are supposed to be defined on a bounded domain $\Omega \in \mathbb{R}^d$ for $d = 1, 2$, or 3 with Lipschitz boundary. We ask for a deformation $\phi : \Omega \rightarrow \Omega$ such that $u_T \circ \phi$ is optimally correlated to u_R . In case of matching the intensities we search for ϕ such that $u_T \circ \phi \approx u_R$ reflected by the basic matching energy

$$\mathcal{E}_m[\phi] := \int_{\Omega} |u_T \circ \phi - u_R|^2 \, d\mathcal{L}.$$

As boundary condition we require $\phi = \mathbb{1}$ on $\partial\Omega$. Here, $\mathbb{1}$ indicates the identity mapping on Ω and simultaneously the identity matrix. This corresponding minimization problem is known to be ill posed [12,67]. Thus, we ask for a suitable regularization. Different regularization approaches have been considered in the literature [18,16,26]. Usually, the results presented so far rely on the assumption that the images are smooth. To our knowledge, there are no analytic results for images with sharp edges as they frequently appear in the applications. We are going to address this problem here. As a simple regularization energy the Dirichlet energy

$$\mathcal{E}_{reg}[\phi] := \frac{1}{2} \int_{\Omega} |\mathcal{D}\phi|^2 d\mathcal{L}$$

of the deformation ϕ for $\alpha > 0$ is near at hand. We are aiming to apply the direct method from the calculus of variations [25] to prove existence of a minimizing deformation for the energy $\mathcal{E} := \mathcal{E}_m + \mathcal{E}_{reg}$. Caratheodory's condition is known to be the essential assumption to ensure existence of minimizers for such functionals. This especially requires the continuity of the energy integrand with respect to the argument ϕ and therefore in our case $u_T \in C^0(\overline{\Omega})$. Real images frequently contain edges where the image intensity jumps, and hence such images are not continuous and the Caratheodory condition is not fulfilled. Indeed, a more appropriate function space for images would be a space which allows images to have edge discontinuities (cf. the Mumford and Shaw approach to image processing [56,53]). Here, we consider the space of bounded functions I being continuous up to a singular set S_I . We suppose that for the Lebesgue measure $\mathcal{L}(\cdot)$

$$\mathcal{L}(B_\varepsilon(S_I)) \xrightarrow{\varepsilon \rightarrow 0} 0$$

holds. Let us introduce a corresponding function space

$$\mathcal{T}^0(\Omega) := \left\{ u : \Omega \rightarrow \mathbb{R} \mid u \in L^\infty, \exists S_u \subset \Omega \text{ s. t. } u \in C^0(\Omega \setminus S_u), \mathcal{L}(B_\varepsilon(S_u)) \xrightarrow{\varepsilon \rightarrow 0} 0 \right\}.$$

To exemplify the difficulties of the above stated basic matching problem we will study the following illustrative 1D problem in detail:

Example 11 *Let us consider images*

$$u_T^\delta = \text{sign}_\delta(x) := \begin{cases} -1 & ; x < -\delta \\ \frac{x}{\delta} & ; x \in [-\delta, \delta] \\ 1 & ; x > \delta \end{cases}$$

for some fixed $\delta \geq 0$ and $u_R \equiv 0$ on $\Omega = (-1, 1)$ for $d = 1$. Obviously, the energy infimum zero can only be attained if $\phi = 0$ a. e., and therefore \mathcal{E}_m has no minimizer ϕ which is C^0 and fulfills the boundary conditions. Indeed, a minimizing sequence $\{\phi_k\}_{k=0,1,\dots} \subset C^0$ can be selected such that $\mathcal{E}_m[\phi_k] \rightarrow 0$. But the convergence $\phi_k \rightarrow 0$ is not uniform. If we now consider regularized images u_T^δ with $\delta > 0$, we observe that the Euler Lagrange equation for a solutions $\phi_{\alpha,\delta}$ of the minimizing problem

$$\mathcal{E}_m[\phi] + \alpha \mathcal{E}_{reg}[\phi] \rightarrow \min$$

leads to $\phi_{\alpha,\delta}'' = 0$ for $|\phi_{\alpha,\delta}| > \delta$ and $\phi_{\alpha,\delta}'' = \frac{2}{\alpha\delta^2}\phi_{\alpha,\delta}$ for $|\phi_{\alpha,\delta}| < \delta$. Hence, $\phi_{\alpha,\delta}(x) = \gamma_{\alpha,\delta} \sinh(\frac{\sqrt{2}x}{\sqrt{\alpha\delta}})$ on $[-y_{\alpha,\delta}, y_{\alpha,\delta}]$ for some constant $\gamma_{\alpha,\delta}$ and $\phi_{\alpha,\delta}(x) = \text{sign}(x)(\delta + \frac{1-\delta}{1-y_{\alpha,\delta}}(|x| - y_{\alpha,\delta}))$ elsewhere. Here, $y_{\alpha,\delta}$ is the pre-image of δ , i. e. $\phi_{\alpha,\delta}(y_{\alpha,\delta}) = \delta$, and finally we have in addition $\phi_{\alpha,\delta}'(y_{\alpha,\delta} + 0) = \phi_{\alpha,\delta}'(y_{\alpha,\delta} - 0)$. One easily verifies that these conditions uniquely define $y_{\alpha,\delta}$ as the root of

$$q(y, \alpha, \delta) = \frac{1-\delta}{1-y} - \frac{\sqrt{2}}{\sqrt{\alpha}} \text{cotanh}\left(\frac{\sqrt{2}y}{\sqrt{\alpha\delta}}\right)$$

on $(0, 1)$. Indeed, because $\lim_{y \rightarrow 0+0} q(y, \alpha, \delta) = -\infty$ and $\lim_{y \rightarrow 1-0} q(y, \alpha, \delta) = \infty$, there is a root for any $\alpha > 0$ and any $\delta \in (0, 1)$, and from the uniqueness of the solution of the Euler Lagrange equation we deduce that this root is unique. To explore the solution behavior for different values of α and δ let us derive upper and lower bounds for $y_{\alpha,\delta}$. We estimate

$$\begin{aligned} \bar{\mathcal{E}} &:= \mathcal{E}[\mathbb{1}] \geq \mathcal{E}[\phi_{\alpha,\delta}] \geq \alpha \mathcal{E}_{\text{reg}}[\phi_{\alpha,\delta}] \\ &= \frac{\alpha}{2} \int_{-1}^1 |\phi_{\alpha,\delta}'|^2 = -\frac{\alpha}{2} \int_{-1}^1 \phi_{\alpha,\delta}'' \phi_{\alpha,\delta} + \frac{\alpha}{2} [\phi_{\alpha,\delta}' \phi_{\alpha,\delta}]_{-1}^1 \geq \alpha \frac{1-\delta}{1-y_{\alpha,\delta}} - 2 \end{aligned}$$

and claim $y_{\alpha,\delta} \leq 1 - \alpha \frac{1-\delta}{\bar{\mathcal{E}}+2}$. Furthermore, the total energy of the function

$$\psi = \begin{cases} 0 & ; |x| \leq 1 - \sqrt{\frac{\alpha}{2}} \\ \text{sign}(x)(1 - \sqrt{\frac{2}{\alpha}}(1 - |x|)) & ; \text{else} \end{cases}$$

turns out to be bounded from above by $2\sqrt{2\alpha}$, and the matching energy $\mathcal{E}_m[\phi_{\alpha,\delta}]$ is bounded from below by $2(1 - y_{\alpha,\delta})$. Thus $y_{\alpha,\delta} \geq 1 - \sqrt{2\alpha}$. As a consequence we observe that on $[-1 + \sqrt{2\alpha}, 1 - \sqrt{2\alpha}]$, the family of minimizers $\phi_{\alpha,\delta} \rightarrow 0$ uniformly for $\delta \rightarrow 0$. This clearly outlines a disadvantage of the regularization via a Dirichlet integral: If we approximate u_T^0 by the continuous images u_T^δ , the Lebesgue measure of the pre-image of a neighborhood of the template singularity set $S_{u_T^0}$ can not be uniformly controlled for the corresponding minimizing deformation.

The Example 11 underlines that in case of a Dirichlet regularization energy it seems to be impossible to control the measure of the pre-image of arbitrarily small edge neighborhoods of the image u_T . Hence, it can not be ruled out that small regions containing the singularities of the image u_T are referred by large regions with respect to their pre-image under the mapping ϕ . Beyond this, one can not rule out selfintersection on the image domain. We ask for a new regularization energy which in particular allows to control volume shrinkage and simultaneously ensures continuity and injectivity for the minimizing deformation. The nonlinear polyconvex elastic energies of the above type fulfill these requirements. The existence proof for minimizers of nonlinear elastic energies via the calculus of variations and direct methods dates back to the work of J. Ball [6]. Especially the incorporated control of the volume transformation in this theory turns out to be the key to prove existence of minimizing, continuous, and injective

deformations for the image matching problem discussed here. Let us denote by L^p for $p \in [1, \infty]$ the usual Lebesgue spaces of functions on Ω into \mathbb{R} , \mathbb{R}^d and $u_R^{d,d}$ respectively, by $|\cdot|_p$ the corresponding norm, and by $H^{1,p}$ the Hilbert space of functions in L^p with weak first derivatives also in L^p . For the ease of presentation, we do not exploit the full generality of the corresponding existence theory. Here the reader is for instance referred to [6,7,68,36,20]. We confine to a basic model and state the following theorem:

Theorem 12 (Existence of minimizing deformations) *Suppose $d = 3$,*

$$u_T, u_R \in \mathcal{I}^0(\Omega),$$

and consider a matching energy $\mathcal{E}_m[\phi] = \int_{\Omega} |u_T \circ \phi - u_R|^2$, a regularization energy

$$\mathcal{E}_{elast}[\phi] = \int_{\Omega} W(|\mathcal{D}\phi|^2, |\text{cof}\mathcal{D}\phi|^2, \det\mathcal{D}\phi) d\mathcal{L},$$

and the total energy $\mathcal{E}[\phi] = \mathcal{E}_m[\phi] + \mathcal{E}_{elast}[\phi]$ for deformations ϕ in the set of admissible deformations

$$\begin{aligned} \mathcal{A} := \{ \phi : \Omega \rightarrow \Omega \mid \phi \in H^{1,p}(\Omega), \text{cof}\mathcal{D}\phi \in L^q(\Omega), \\ \det\mathcal{D}\phi \in L^r(\Omega), \det\mathcal{D}\phi > 0 \text{ a.e. in } \Omega, \phi = \mathbb{1} \text{ on } \partial\Omega \} \end{aligned}$$

where $p, q > 3$ and $r > 1$. Furthermore, suppose $W : \mathbb{R} \times \mathbb{R} \times \mathbb{R} \rightarrow \mathbb{R}$ is convex, and there exist constants $\beta, s \in \mathbb{R}$, $\beta > 0$, and $s > \frac{2q}{q-3}$ such that

$$W(I_1, I_2, I_3) \geq \beta(I_1^{\frac{p}{2}} + I_2^{\frac{q}{2}} + I_3^r + I_3^{-s}) \quad \forall I_1, I_2 \in \mathbb{R}, I_3 \in \mathbb{R}^+. \quad (10)$$

Then $\mathcal{E}[\phi]$ attains its minimum over all deformation $\phi \in \mathcal{A}$, the minimizing deformation ϕ is a homeomorphism and in particular $\det\mathcal{D}\phi > 0$ a.e. in Ω .

Proof The proof of this result is based on the observation that the volume of the pre-image $\phi^{-1}(B_\varepsilon(S_T))$ of an ε -neighborhood of the singularity set S_T of the image u_T can be controlled. At first, let us recall some well known, fundamental weak convergence results:

Let $(\phi^k)_k$ be a sequence of deformations in $H^{1,p}$ with $\text{cof}\mathcal{D}\phi^k \in L^q$ and $\det\mathcal{D}\phi^k \in L^r$, such that the sequence convergence weakly in the sense $\phi^k \rightharpoonup \phi$ in $H^{1,p}$, $\text{cof}\mathcal{D}\phi^k \rightharpoonup C$ in L^q and $\det\mathcal{D}\phi^k \rightharpoonup D$ in L^r , then $C = \text{cof}\mathcal{D}\phi$ and $D = \det\mathcal{D}\phi$ (weak continuity).

For the proof of these fundamental results we refer to Ball [6] or the book of Ciarlet [19] (Section 7.5, 7.6). The proof of the theorem proceeds in 4 steps:

Step 1. We observe $\mathbb{1} \in \mathcal{A}$, thus $\underline{\mathcal{E}} := \inf_{\phi \in \mathcal{A}} \mathcal{E}[\phi] < \infty$. Next we observe that $\mathcal{E}[\cdot]$ is well defined for every $\phi \in \mathcal{A}$. Let us consider a minimizing sequence $(\phi^k)_{k=0,1,\dots}$ in \mathcal{A} with $\mathcal{E}[\phi^k] \rightarrow \inf_{\phi \in \mathcal{A}} \mathcal{E}[\phi]$. We denote by $\bar{\mathcal{E}}$ an upper bound of the energy \mathcal{E} on this sequence. Due to the growth condition on W we get that

$$\left\{ (\mathcal{D}\phi^k, \text{cof}\mathcal{D}\phi^k, \det\mathcal{D}\phi^k) \right\}_{k=0,1,\dots}$$

is uniformly bounded in $L^p \times L^q \times L^r$. By Poincaré's inequality applied to $(\phi^k - \mathbb{1})$ we obtain that $\{\phi^k\}_{k=0,1,\dots}$ is uniformly bounded in $H^{1,p}(\Omega)$. Because of the reflexivity

of $L^p \times L^q \times L^r$ for $p, q, r > 1$ we can extract a weakly convergent subsequence, again denoted by an index k , such that

$$(\mathcal{D}\phi^k, \text{cof } \mathcal{D}\phi^k, \det \mathcal{D}\phi^k) \rightharpoonup (D\phi, C, D)$$

in $L^p \times L^q \times L^r$ with $C : \Omega \rightarrow \mathbb{R}^{3 \times 3}$, $D : \Omega \rightarrow \mathbb{R}$. Applying the above results on weak convergence we achieve $C = \text{cof } \mathcal{D}\phi$ and $D = \det \mathcal{D}\phi$. In addition, by Rellich's embedding theorem we know that $\phi^k \rightarrow \phi$ strongly in $L^p(\Omega)$ and by Sobolev's embedding theorem we claim $\phi \in C^0(\bar{\Omega})$.

Step 2. Next, we control the set where the volume shrinks by a factor of more than ε^{-1} for the limit deformation. Let us define

$$S_\varepsilon = \{x \in \Omega : \det \mathcal{D}\phi \leq \varepsilon\}$$

for $\varepsilon \leq \delta_0$. Without loss of generality we assume that the sequence of energy values $\mathcal{E}[\phi^k]$ is monotone decreasing and for given $\varepsilon > 0$ we denote by $k(\varepsilon)$ the smallest index such that

$$\mathcal{E}[\phi^k] \leq \mathcal{E}[\phi^{k(\varepsilon)}] \leq \underline{\mathcal{E}} + \varepsilon \quad \forall k \geq k(\varepsilon).$$

From Step 1 we know that $\Psi^k := (\mathcal{D}\phi^k, \text{cof } \mathcal{D}\phi^k, \det \mathcal{D}\phi^k)$ converges weakly to $\Psi := (D\phi, \text{cof } \mathcal{D}\phi, \det \mathcal{D}\phi)$ in $L^2 \times L^2 \times L^r$. Hence, applying Mazur's Lemma we obtain a sequence of convex combination of Ψ^k which converges strongly to Ψ . I.e. there exists a family of weights $((\lambda_i^k)_{k(\varepsilon) \leq i \leq k})_{k \geq k(\varepsilon)}$ with $\lambda_i^k \geq 0$, $\sum_{k(\varepsilon)}^k \lambda_i^k = 1$, such that

$$\lambda_i^k \Psi^i \rightarrow \Psi \quad \text{and} \quad \lambda_i^k \phi^i \rightarrow \phi.$$

Here and in what follows we make use of the summation convention. Now, using especially the properties of Γ , the convexity of W and Fatou's lemma we estimate

$$\begin{aligned} \beta \varepsilon^{-s} \mathcal{L}(S_\varepsilon) &\leq \beta \int_{S_\varepsilon} (\det \mathcal{D}\phi)^{-s} d\mathcal{L} \leq \int_{S_\varepsilon} W(\Psi) d\mathcal{L} \\ &= \int_{S_\varepsilon} \liminf_{k \rightarrow \infty} W(\lambda_i^k \Psi^i) d\mathcal{L} \leq \int_{S_\varepsilon} \liminf_{k \rightarrow \infty} \lambda_i^k W(\Psi^i) d\mathcal{L} \\ &\leq \liminf_{k \rightarrow \infty} \lambda_i^k \int_{S_\varepsilon} W(\Psi^i) d\mathcal{L} \leq \liminf_{k \rightarrow \infty} \lambda_i^k \int_{\Omega} W(\Psi^i) + (u_T \circ \phi^i - u_R)^2 d\mathcal{L} \\ &\leq \bar{\mathcal{E}} \end{aligned}$$

and claim $\mathcal{L}(S_\varepsilon) \leq \frac{\bar{\mathcal{E}} \varepsilon^s}{\beta}$. As a consequence S_0 is a null set and we know that $\det \mathcal{D}\phi > 0$ a. e. on Ω . Thus, together with the results from Step 1 we deduce that the limit deformation ϕ is in the set of admissible deformations \mathcal{A} . Following Ball [7] we furthermore obtain that ϕ is injective. Hence, ϕ is a homeomorphism.

Step 3. Now, we deal with the singularity sets of the images u_T, u_R . By our assumption on the image space $\mathcal{I}^0(\Omega)$ we know that for given $\delta > 0$ there exist $\varepsilon_T, \varepsilon_R > 0$ such

that $\mathcal{L}(B_{\varepsilon_T}(S_T)), \mathcal{L}(B_{\varepsilon_R}(S_R)) \leq \delta$. From this and the injectivity (cf. Theorem 1 (ii) in [7]) we deduce the estimate

$$\mathcal{L}(\phi^{-1}(B_{\varepsilon_T}(S_T)) \setminus S_\varepsilon) \leq \frac{1}{\varepsilon} \int_{\phi^{-1}(B_{\varepsilon_T}(S_T))} \det \mathcal{D}\phi \, d\mathcal{L} = \frac{1}{\varepsilon} \int_{B_{\varepsilon_T}(S_T)} d\mathcal{L} \leq \frac{\delta}{\varepsilon}.$$

Hence, we can control the pre-image of $B_\varepsilon(S_T)$ with respect to ϕ restricted to $\Omega \setminus S_\varepsilon$, i.e.

$$\mathcal{L}(\phi^{-1}(B_{\varepsilon_T}(S_T)) \setminus S_\varepsilon) \leq \frac{\delta}{\varepsilon}$$

Step 4. Due to Egorov's theorem and the strong convergence of ϕ^k in $L^p(\Omega)$ there is a set K_ε with $\mathcal{L}(K_\varepsilon) < \varepsilon$ such that ϕ^k converges uniformly on $\Omega \setminus K_\varepsilon$. Let us now define the set

$$R_{\delta,\varepsilon} := \phi^{-1}(B_{\varepsilon_T}(S_T)) \cup B_{\varepsilon_R}(S_R) \cup S_\varepsilon \cup K_\varepsilon,$$

whose measure can be estimated in terms of ε and δ , i.e.

$$\mathcal{L}(R_{\delta,\varepsilon}) \leq \frac{\delta}{\varepsilon} + \delta + \frac{\tilde{\mathcal{E}}\varepsilon^s}{\beta} + \varepsilon.$$

On $\Omega \setminus R_{\delta,\varepsilon}$ the sequence $(u_T \circ \phi^k - u_R)_{k=0,1,\dots}$ converges uniformly to $u_T \circ \phi - u_R$. From the above control of the pre-image of $B_{\varepsilon_T}(S_T)$ we deduce the measurability of $u_T \circ \phi - u_R$ (cf. equation 1.4). Obviously, the integral $\int_\Omega |u_T \circ \phi - u_R|^2$ is bounded by $C_\infty \mathcal{L}(\Omega)$ with

$$C_\infty := 2(|u_T|_\infty^2 + |u_R|_\infty^2).$$

We choose $k(\varepsilon)$ large enough to ensure that

$$|u_T \circ \phi^k(x) - u_R(x)|^2 - |u_T \circ \phi(x) - u_R(x)|^2 \leq \varepsilon$$

for $x \in \Omega \setminus R_{\delta,\varepsilon}$ and $\forall k \geq k(\varepsilon)$. Now we are able to estimate $\mathcal{E}[\phi]$ using especially the convexity of W and Fatou's lemma:

$$\begin{aligned} \mathcal{E}[\phi] &= \int_\Omega W(\Psi) + |u_T \circ \phi - u_R|^2 \, d\mathcal{L} \\ &\leq \int_\Omega W(\lim_{k \rightarrow \infty} \lambda_i^k \Psi^i) \, d\mathcal{L} + \int_{\Omega \setminus R_{\delta,\varepsilon}} |u_T \circ \phi - u_R|^2 \, d\mathcal{L} + C_\infty \mathcal{L}(R_{\delta,\varepsilon}) \\ &\leq \int_\Omega \liminf_{k \rightarrow \infty} \lambda_i^k W(\Psi^i) \, d\mathcal{L} + \liminf_{k \rightarrow \infty} \lambda_i^k \int_{\Omega \setminus R_{\delta,\varepsilon}} |u_T \circ \phi^i - u_R|^2 \, d\mathcal{L} + \\ &\quad \varepsilon \mathcal{L}(\Omega) + C_\infty \mathcal{L}(R_{\delta,\varepsilon}) \\ &\leq \liminf_{k \rightarrow \infty} \lambda_i^k \int_\Omega W(\Psi^i) + |u_T \circ \phi^i - u_R|^2 \, d\mathcal{L} + \varepsilon \mathcal{L}(\Omega) + 2C_\infty \mathcal{L}(R_{\delta,\varepsilon}) \\ &= \liminf_{k \rightarrow \infty} \lambda_i^k \mathcal{E}[\phi^i] + \varepsilon \mathcal{L}(\Omega) + 2C_\infty \mathcal{L}(R_{\delta,\varepsilon}) \\ &\leq \underline{\mathcal{E}} + \varepsilon + \varepsilon \mathcal{L}(\Omega) + 2C_\infty \mathcal{L}(R_{\delta,\varepsilon}). \end{aligned}$$

Finally, for given $\bar{\varepsilon}$ we choose ε and then δ and the dependent $\varepsilon_T, \varepsilon_R$ small enough to ensure that

$$\varepsilon + \varepsilon \mathcal{L}(\Omega) + 2C_\infty \left(\varepsilon + \frac{\bar{\varepsilon} \varepsilon^s}{\beta} \right) \leq \frac{\bar{\varepsilon}}{2}, \quad 2C_\infty \left(\frac{\delta}{\varepsilon} + \delta \right) \leq \frac{\bar{\varepsilon}}{2}.$$

and get $\mathcal{E}[\phi] \leq \underline{\mathcal{E}} + \bar{\varepsilon}$. This holds true for an arbitrary choice of $\bar{\varepsilon}$. Thus we conclude with the desired result

$$\mathcal{E}[\phi] \leq \underline{\mathcal{E}} = \inf_{\varphi \in \mathcal{A}} \mathcal{E}[\varphi].$$

□

Let us remark that for the case of two dimensional image matching problems an analogous results holds true. Hence, we skip the dependency of the regularization energy on $\text{cof } \mathcal{D}\phi$ and occasionally weaken the growth conditions. Theorem 12 can be regarded as a generalization of Theorem 3 in [7] with respect to forces with discontinuities. Indeed, some further simple generalization of the external force term - here encoding the derivative of the matching energy - is straightforward.

Space discretization of nonlinear elasticity In what follows we will briefly comment on the variation and the spatial discretization of the energy $\mathcal{E}_{elast}[\cdot]$. For the variation we obtain

$$\langle \delta_\phi \mathcal{E}_{elast}[\phi], \psi \rangle = \int_{\Omega} W_{,A}(\mathcal{D}\phi) : \mathcal{D}\psi \, d\mathcal{L}$$

for a vector valued displacement type test functions ψ . Concerning the polyconvex energy integrand given in (8) and (9), we obtain

$$\begin{aligned} W_{,A}(A) : B &= 2 \partial_{I_1} \bar{W}(|A|^2, |\text{cof } A|^2, \det A) A : B + \\ & 2 \partial_{I_2} \bar{W}(|A|^2, |\text{cof } A|^2, \det A) \text{cof } A : \partial_A \text{cof}(A)(B) + \\ & \partial_{I_3} \bar{W}(|A|^2, |\text{cof } A|^2, \det A) \partial_A \det(A)(B), \end{aligned}$$

where

$$\begin{aligned} \partial_A \det(A)(B) &= \det(A) \text{tr}(A^{-1}B), \\ \partial_A \text{cof}(A)(B) &= \det(A) \text{tr}(A^{-1}B) A^{-T} - \det A A^{-T} B^T A^{-T}, \\ \partial_{I_1} \bar{W}(I_1, I_2, I_3) &= \frac{p}{2} \alpha_1 (I_1 - d)^{\frac{p-2}{2}}, \\ \partial_{I_2} \bar{W}(I_1, I_2, I_3) &= \frac{q}{2} \alpha_2 (I_2 - d)^{\frac{q-2}{2}}, \\ \partial_{I_3} \bar{W}(I_1, I_2, I_3) &= s \alpha_3 (I_3^{-1} - I_3^{-s-1}). \end{aligned}$$

If we now consider a discrete deformation ϕ in the finite element space \mathcal{V}^d , we can evaluate the nodal vector of the L^2 gradient of the energy

$$\mathcal{E}_{elast}[\Phi] = \int_{\Omega} \hat{W}(\mathcal{D}\Phi) \, d\mathcal{L}$$

by

$$(\text{grad}_{L^2} \mathcal{E}_{\text{elast}}[\bar{\Phi}])_{ij} = (M[\mathbb{1}] (\int_{\Omega} \hat{W}_{,A}(\mathcal{D}\Phi) : e_i \Theta_j d\mathcal{L})_j)_i$$

where $M[\mathbb{1}]$ is the usual mass matrix, e_i the i th canonical unit vector, and Θ_j one of the basis functions of \mathcal{V} .

2 Matching geometries and image morphologies

Now we will start the discussion of morphological image matching, where instead of a direct comparison of image intensities we compare local image morphologies. At first we focus on a matching of the regular morphology, followed by a discussion of a pur
[MR:

ich habe das Wort pur im Wörterbuch nicht gefunden] of the edge sets. Finally, full joint models will be investigated.

2.1 Matching ensembles of level sets

In this section we will construct a suitable matching energy, which measures the defect of the morphology of the reference image u_R and the deformed template image u_T . Thus, with respect to the above identification of morphologies and normal fields we ask for a deformation ϕ such that

$$n_T \circ \phi \parallel n_R^\phi, \quad (11)$$

where n_R^ϕ is the transformed normal n_R of the reference image u_R on $T_{\phi(x)}\phi([u_R(x)])$ and n_T the normal of the template image u_T ; both are evaluated at position x . We have already seen, that the deformed normal is given by

$$n_R^\phi = \frac{\text{cof } \mathcal{D}\phi n_R}{|\text{cof } \mathcal{D}\phi n_R|}$$

In a variational setting, optimality can be expressed in terms of energy minimization. Hence, we consider a matching energy

$$\mathcal{E}_{GM}[\phi] := \int_{\Omega} g(n_T \circ \phi, n_R, \text{cof } \mathcal{D}\phi) d\mathcal{L}$$

for some function $g : S^{d-1} \times S^{d-1} \times \mathbb{R}^{d,d} \rightarrow \mathbb{R}^+$; $(u, v, A) \mapsto g(u, v, A)$. Here S^{d-1} denotes the unit sphere in \mathbb{R}^d . As boundary condition we require $\phi = \mathbb{1}$ on $\partial\Omega$. To be not too restrictive with respect to the space of images we have to take into account the problem of degenerate Gauss maps. Hence, let us recall the set $F[u] := \{x \in \Omega : \nabla u = 0\}$ for $u = u_T$ or $u = u_R$, where no image normal can be defined. At first, we resolve this problem of undefined normals at least formally by introducing a 0-homogeneous extension $g_0 : \mathbb{R}^d \times \mathbb{R}^d \times \mathbb{R}^{d,d} \rightarrow \mathbb{R}^+$ of g in the first and second argument:

$$g_0(v, w, A) = \begin{cases} 0 & ; \quad v = 0 \text{ or } w = 0 \\ g(\frac{v}{|v|}, \frac{w}{|w|}, A) & ; \quad \text{else} \end{cases}. \quad (12)$$

Based on g_0 we can redefine the matching energy \mathcal{E}_{GM} and obtain

$$\mathcal{E}_{GM}[\phi] := \int_{\Omega} g_0(\nabla u_T \circ \phi, \nabla u_R, \text{cof } \mathcal{D}\phi) \, d\mathcal{L}. \quad (13)$$

In the later analysis we have to take special care of the singularity of g_0 for vanishing first or second argument. Indeed, we will assume that the measure of $F[u_T]$ and $F[u_R]$ is in a suitable sense sufficiently small. Furthermore, in the existence theory we will explicitly control the impact of these sets on the energy. As a first choice for the energy density g let us consider

$$g(v, w, A) := \left(v - \frac{Aw}{|Aw|} \right)^2 \quad (14)$$

for $v, w \in S^{d-1}$, which corresponds to the energy

$$\int_{\Omega} |n_T \circ \phi - n_R^\phi|^2.$$

We observe that the energy \mathcal{E}_{GM} vanishes if $u_T \circ \phi = \gamma \circ u_R$ for a monotone grey value transformation $\gamma: \mathbb{R} \rightarrow \mathbb{R}$. If we want \mathcal{E}_{GM} to vanish also for non-monotone transformations γ we are lead to the symmetry assumption:

$$g(v, w, A) = g(-v, w, A) = g(v, -w, A). \quad (15)$$

Example 21 *A useful class of matching functionals \mathcal{E}_{GM} is obtained by choosing functions g which depend on the scalar product $v \cdot u$ or alternatively on $(\mathbb{1} - v \otimes v)u$ (where $\mathbb{1} - v \otimes v = (\delta_{ij} - v_i v_j)_{ij}$ denotes the projection of u onto the plane normal to v) for $u = \frac{Aw}{|Aw|}$ and $v, w \in S^{d-1}$, i. e.,*

$$g(v, w, A) = \hat{g} \left((\mathbb{1} - v \otimes v) \frac{Aw}{|Aw|} \right). \quad (16)$$

Let us remark that $\hat{g}((\mathbb{1} - v \otimes v)u)$ is convex in u , if \hat{g} is convex. With respect to arbitrary grey value transformations mapping morphologically identical images onto each other, we might consider $\hat{g}(s) = |s|^\gamma$ for some $\gamma \geq 1$.

Let us now discuss under which conditions there exists a minimizing deformation of the total energy $\mathcal{E}[\cdot]$ if we add a hyperelastic regularization energy $\mathcal{E}_{elast}[\phi]$. Let us emphasize that the problem stated here significantly differs from most other regularized image registration problems, e. g., all intensity based approaches, where the matching energy is defined solely in terms of the deformation ϕ , and the regularization energy is of higher order and considers the Jacobian $\mathcal{D}\phi$ of the deformation. In our case already the matching energy incorporates the cofactor of the Jacobian. Thus, with respect to the direct method in the calculus of variations, we can not use standard compactness arguments due to Rellich's Embedding Theorem to deal with the matching energy on a minimizing sequence [25]. Instead, we will need suitable convexity assumptions on the function g .

Remark 22 (Lack of lower semicontinuity for certain functionals \mathcal{E}_{GM}) Recalling Example 21 we might wish to choose a matching energy with an integrand $g_0(v, w, A) := \hat{g}((\mathbb{1} - \frac{v}{|v|} \otimes \frac{v}{|v|}) \frac{Aw}{|Aw|})$ for $\hat{g} \in C^0(\mathbb{R}^d, \mathbb{R}_0^+)$. It is well known that the essential condition to ensure weak sequential lower semicontinuity of functionals depending on the Jacobian of a deformation is quasiconvexity [54,55]. With our special choice of the class of energies (13) this requires the convexity of g in the argument A (cf. [25] Section 5.1). Indeed, we easily verify that a function

$$f : \mathbb{R}^{d,d} \rightarrow \mathbb{R}; A \mapsto f(A)$$

which is 0-homogeneous on $\mathbb{R}^{d,d}$ and convex has to be constant and thus an existence result for our image matching problem via the direct calculus of variations can only be expected for trivial matching energies, i. e., for $\hat{g} \equiv \text{const}$. To see this, suppose $A, B \in \mathbb{R}^{d,d}$ with $f(A) - f(B) = \delta > 0$. Using the definition $A_{\alpha,r} := rA + \alpha(A - B)$ for $r > 0$, $\alpha > 0$ and setting $s = \frac{\alpha}{r}$, we obtain

$$\begin{aligned} f(A_{\alpha,r}) &= f(rA + sr(A - B)) \\ &\geq f(rA) + s(f(rA) - f(rB)) \\ &= f(A) + \frac{\alpha}{r}(f(A) - f(B)) = f(A) + \frac{\alpha \delta}{r} \rightarrow \infty \end{aligned}$$

for $r \rightarrow 0$. Finally, we deduce $f(A - B) = \infty$ which contradicts our assumptions on f . Thus, the definition of the matching energy via the above integrand $\hat{g}((\mathbb{1} - v \otimes v) \frac{Aw}{|Aw|})$ and especially our first choice of a matching energy in (14) is not appropriate with respect to a positive answer to the question of existence of minimizers via direct methods.

Next, we take into account the singularities of the normal fields. We require, that

$$\mathcal{L}(B_\varepsilon(\partial F[u])) \xrightarrow{\varepsilon \rightarrow 0} 0,$$

for u either u_R or u_T . The corresponding set of image intensity functions is then given by

$$\mathcal{I}(\Omega) := \left\{ u : \Omega \rightarrow \mathbb{R} : u \in C^1(\bar{\Omega}), \mathcal{L}(B_\varepsilon(\partial F[u])) \xrightarrow{\varepsilon \rightarrow 0} 0 \right\}$$

The existence proof for minimizers of nonlinear elastic energies via the calculus of variations and direct methods dates back to the work of J. Ball [6]. Especially the incorporated control of the volume transformation in this theory turns out to be the key to prove existence of minimizing, continuous and injective deformations for the image matching problem discussed here. We consider the following energy (cf. equations (13) and (8)):

$$\mathcal{E}[\phi] := \mathcal{E}_{GM}[\phi] + \mathcal{E}_{elast}[\phi]. \quad (17)$$

Theorem 23 (Existence of minimizing deformations) Suppose $d = 3$, $u_T, u_R \in \mathcal{I}(\Omega)$ and consider the total energy defined in (17) for deformations ϕ in the set of admissible deformations

$$\begin{aligned} \mathcal{A} := \{ \phi : \Omega \rightarrow \Omega \mid &\phi \in H^{1,p}(\Omega), \text{cof } \mathcal{D}\phi \in L^q(\Omega), \\ &\det \mathcal{D}\phi \in L^r(\Omega), \det \mathcal{D}\phi > 0 \text{ a.e. in } \Omega, \phi = \mathbb{1} \text{ on } \partial\Omega \} \end{aligned}$$

where $p, q > 3$ and $r > 1$. Suppose $W : \mathbb{R} \times \mathbb{R} \times \mathbb{R}^+ \rightarrow \mathbb{R}$ is convex, and there exist constants $\beta, s \in \mathbb{R}$, $\beta > 0$, and $s > \frac{2q}{q-3}$ such that $W(I_1, I_2, I_3) \geq \beta (I_1^{\frac{2}{p}} + I_1^{\frac{2}{q}} + I_3^r + I_3^{-s})$.

Furthermore, assume that $g_0(v, w, A) = g(\frac{v}{|v|}, \frac{w}{|w|}, A)$, for some function $g : S^2 \times S^2 \times \mathbb{R}^{3,3} \rightarrow \mathbb{R}_0^+$, which is continuous in $\frac{v}{|v|}, \frac{w}{|w|}$, convex in A and for a constant $m < q$ and a constant $C_g > 0$ the estimate

$$g(v, w, A) - g(u, w, A) \leq C_g |v - u| (1 + |A|^m)$$

holds for a constant $m < q$, for all $u, v, w \in S^2$ and $A \in \mathbb{R}^{3,3}$. Then $\mathcal{E}[\cdot]$ attains its minimum over all deformations $\phi \in \mathcal{A}$, and the minimizing deformation ϕ is a homeomorphism and in particular $\det \mathcal{D}\phi > 0$ a.e. in Ω .

Proof The proof of this result proceeds first along the lines of the proof of Theorem 12. Here, the critical is not the set of discontinuities of the images but the boundaries of the sets of degenerate normals $\partial F[u_T] \cap \partial F[u_R]$. We observe that the total energy is polyconvex. Furthermore, as in Theorem 12 the volume of the neighborhood sets of the singularity sets can be controlled. Hence, we can basically confine to a set, where the integrand fulfills Carathéodory's conditions. The proof of the theorem proceeds in 3 steps:

Step 1. Due to the assumption on the image, the set $\mathcal{I}(\Omega) \mathcal{E}_{GM}[\phi]$ is well defined for $\phi \in \mathcal{A}$. In particular $g_0(\nabla u_T \circ \phi, \nabla u_R, \text{cof } \mathcal{D}\phi)$ is measurable. Obviously, $\mathbb{1} \in \mathcal{A}$ and $\mathcal{E}[\mathbb{1}] < \infty$, thus $\underline{\mathcal{E}} := \inf_{\phi \in \mathcal{A}} \mathcal{E}[\phi] < \infty$, and due to the growth conditions and the assumption of g we furthermore get $\underline{\mathcal{E}} \geq 0$. Let us consider a minimizing sequence $(\phi^k)_{k=0,1,\dots} \subset \mathcal{A}$ with $\mathcal{E}[\phi^k] \rightarrow \inf_{\phi \in \mathcal{A}} \mathcal{E}[\phi]$. We denote by $\bar{\mathcal{E}}$ an upper bound of the energy \mathcal{E} on this sequence. At first, let us recall as in the proof of theorem 12 that for a minimizing sequence, $(\phi^k)_k$ we have $\phi^k \rightharpoonup \phi$ in $H^{1,p}$, $\text{cof } \mathcal{D}\phi^k \rightharpoonup \text{cof } \mathcal{D}\phi$ in L^q and $\det \mathcal{D}\phi^k \rightharpoonup \det \mathcal{D}\phi$ in L^r . In addition, $\phi^k \rightarrow \phi$ strongly in $L^p(\Omega)$ and by Sobolev's embedding theorem we obtain $\phi \in C^0(\bar{\Omega})$.

Step 2. Again, we control the set $S_\varepsilon = \{x \in \Omega : \det \mathcal{D}\phi \leq \varepsilon\}$, where the volume shrinks by a factor of more than ε for the limit deformation. Let us assume without loss of generality that the sequence of energy values $\mathcal{E}[\phi^k]$ is monotone decreasing and that for given $\varepsilon > 0$ we let $k(\varepsilon)$ be the smallest index such that $\mathcal{E}[\phi^k] \leq \mathcal{E}[\phi^{k(\varepsilon)}] \leq \underline{\mathcal{E}} + \varepsilon$ for all $k \geq k(\varepsilon)$. Then as in the proof of Theorem 12 we deduce $\mathcal{L}(S_\varepsilon) \leq \frac{\bar{\mathcal{E}} \varepsilon^s}{\beta}$. As one consequence, S_0 is a null set and we know that $\det \mathcal{D}\phi > 0$ a. e. on Ω and hence the limit deformations ϕ is in the set of admissible deformation \mathcal{A} . In addition, ϕ is injective and a homeomorphism. Furtheron, as in the proof of Theorem 12 we obtain that $\mathcal{L}(\phi^{-1}(B_{\varepsilon_T}(\partial F[u_T] \cap \partial F[u_R]) \setminus S_\varepsilon)) \leq \frac{\delta}{\varepsilon}$. Due to the continuous differentiability of both images u_T and u_R we can assume that

$$|\nabla u_T(x)| \geq \gamma(\varepsilon) \text{ on } \Omega \setminus B_\varepsilon(\partial F[u_T] \cap \partial F[u_R]) \quad (18)$$

where $\gamma : \mathbb{R}_0^+ \rightarrow \mathbb{R}$ is a strictly monotone function with $\gamma(0) = 0$.

Step 3. Due to Egorov's theorem and the strong convergence of ϕ^k in $L^p(\Omega)$ there is a set K_ε with $\mathcal{L}(K_\varepsilon) < \varepsilon$ such that a subsequence, again denoted by ϕ^k , converges uniformly on $\Omega \setminus K_\varepsilon$. Let us now define the set

$$R_{\delta,\varepsilon} := \phi^{-1}(B_{\varepsilon_T}(\partial F[u_T] \cap \partial F[u_R])) \cup S_\varepsilon \cup K_\varepsilon,$$

whose measure can be estimated in terms of ε and δ , i.e.

$$\mathcal{L}(R_{\delta,\varepsilon}) \leq \frac{\delta}{\varepsilon} + \frac{\bar{\mathcal{E}}\varepsilon^s}{\beta} + \varepsilon.$$

On $\Omega \setminus R_{\delta,\varepsilon}$ the sequence $(\nabla u_T \circ \phi^k)_{k=0,1,\dots}$ converges uniformly to $\nabla u_T \circ \phi$. Next, from the assumption on g and the 0-homogeneous extension property of g_0 we deduce that

$$|g_0(u, w, A) - g_0(v, w, A)| \leq C_\gamma |u - v| (1 + |A|^m) \quad (19)$$

for $u, v, w \in \mathbb{R}^3$, $A \in \mathbb{R}^{3,3}$ and $|u|, |v|, |w| \geq \gamma$. Here, C_γ is a constant depending on C_g and on γ . To use this estimate for $u = \phi^k$ and $v = \phi$ below, we assume that $k(\varepsilon)$ is large enough, such that $\phi^k(x) \in \Omega \setminus B_{\frac{\varepsilon_T}{2}}(S_T)$ for $x \in \Omega \setminus R_{\delta,\varepsilon}$ and

$$C_{\gamma(\frac{\varepsilon_T}{2})} \left| \nabla u_T \circ \phi^k - \nabla u_T \circ \phi \right|_{\infty, \Omega \setminus K_\varepsilon} \leq \varepsilon$$

for all $k \geq k(\varepsilon)$. Now we are able to estimate $\mathcal{E}[\phi]$ using especially the convexity of W and $g(v, w, \cdot)$, the estimate (19) and Fatou's lemma:

$$\begin{aligned} \mathcal{E}[\phi] &= \int_{\Omega} W(\Psi) + g_0(\nabla u_T \circ \phi, \nabla u_R, \text{cof } \mathcal{D}\phi) \, d\mathcal{L} \\ &\leq \int_{\Omega} \liminf_{k \rightarrow \infty} \lambda_i^k W(\Psi^i) \, d\mathcal{L} + 2C_g \int_{R_{\delta,\varepsilon}} 1 + |\text{cof } \mathcal{D}\phi|^m \, d\mathcal{L} \\ &\quad + \int_{\Omega \setminus R_{\delta,\varepsilon}} \liminf_{k \rightarrow \infty} \lambda_i^k g_0(\nabla u_T \circ \phi, \nabla u_R, \text{cof } \mathcal{D}\phi^i) \, d\mathcal{L} \\ &\leq \liminf_{k \rightarrow \infty} \lambda_i^k \int_{\Omega} W(\Psi^i) \, d\mathcal{L} + b(\mathcal{L}(R_{\delta,\varepsilon})) \\ &\quad + \liminf_{k \rightarrow \infty} \lambda_i^k \int_{\Omega \setminus R_{\delta,\varepsilon}} g_0(\nabla u_T \circ \phi, \nabla u_R, \text{cof } \mathcal{D}\phi^i) - g_0(\nabla u_T \circ \phi^i, \nabla u_R, \text{cof } \mathcal{D}\phi^i) \\ &\quad \quad + g_0(\nabla u_T \circ \phi^i, \nabla u_R, \text{cof } \mathcal{D}\phi^i) \, d\mathcal{L} \end{aligned}$$

where $b(s) := 2C_g(s + (\frac{\bar{\mathcal{E}}}{\beta})^{\frac{m}{q}} s^{1-\frac{m}{q}})$. Here we have in particular used the a priori estimate $|\text{cof } \mathcal{D}\phi|_{q,\Omega} \leq (\frac{\bar{\mathcal{E}}}{\beta})^{\frac{1}{q}}$. We estimate further and obtain

$$\begin{aligned} \mathcal{E}[\phi] &\leq \liminf_{k \rightarrow \infty} \lambda_i^k \int_{\Omega} W(\Psi^i) + g_0(\nabla u_T \circ \phi^i, \nabla u_R, \text{cof } \mathcal{D}\phi^i) \, d\mathcal{L} + 2b(\mathcal{L}(R_{\delta,\varepsilon})) \\ &\quad + C_{\gamma(\frac{\varepsilon_T}{2})} \sup_{k \rightarrow \infty} \int_{\Omega \setminus R_{\delta,\varepsilon}} \left| \nabla u_T \circ \phi - \nabla u_T \circ \phi^k \right| \left(1 + |\text{cof } \mathcal{D}\phi^k|^m \right) \, d\mathcal{L} \\ &\leq \liminf_{k \rightarrow \infty} \lambda_i^k \mathcal{E}[\phi^i] + 2b(\mathcal{L}(R_{\delta,\varepsilon})) + \varepsilon b(\mathcal{L}(\Omega)) \\ &\leq \underline{\mathcal{E}} + \varepsilon + 2b(\mathcal{L}(R_{\delta,\varepsilon})) + \varepsilon b(\mathcal{L}(\Omega)). \end{aligned}$$

Finally, for given $\bar{\varepsilon}$ we choose ε , δ , the dependent ε_T small enough and $k(\bar{\varepsilon})$ large enough to ensure that

$$\varepsilon + 2b(\mathcal{L}(R_{\delta,\varepsilon})) + \varepsilon b(\mathcal{L}(\Omega)) \leq \bar{\varepsilon}$$

and get $\mathcal{E}[\phi] \leq \underline{\mathcal{E}} + \bar{\varepsilon}$. This holds true for an arbitrary choice of $\bar{\varepsilon}$. Thus we conclude

$$\mathcal{E}[\phi] \leq \underline{\mathcal{E}} = \inf_{\phi \in \mathcal{A}} \mathcal{E}[\phi],$$

which is the desired result. \square

From the proof we have seen that the assumptions on the reference image could be weakened considerably compared to the template image. With respect to the applications we do not detail this difference here. A suitable matching energy density is given by

$$g(v, w, A) = |(\mathbb{1} - v \otimes v)Aw|^\gamma, \quad (20)$$

for $1 \leq \gamma < q$. Hence, we obtain an admissible matching energy

$$\mathcal{E}_{GM}[\phi] = \int_{\Omega} |(\mathbb{1} - (n_T \circ \phi) \otimes (n_T \circ \phi)) \text{cof } \mathcal{D}\phi n_R|^\gamma.$$

Applying Theorem 23, the existence of a minimizing deformation can be established. Recalling Remark 22, we recognize that scaling the original energy density by an additional factor $|\text{cof } \mathcal{D}\phi n_R|^\gamma$ turns the minimization task into a feasible problem. This corresponds to a modification of the area element on the level sets $[u_R = c]$. Indeed, $|\text{cof } \mathcal{D}\phi n_R|$ is the change of the area element at a position x on $[u_R = c]$ under the deformation.

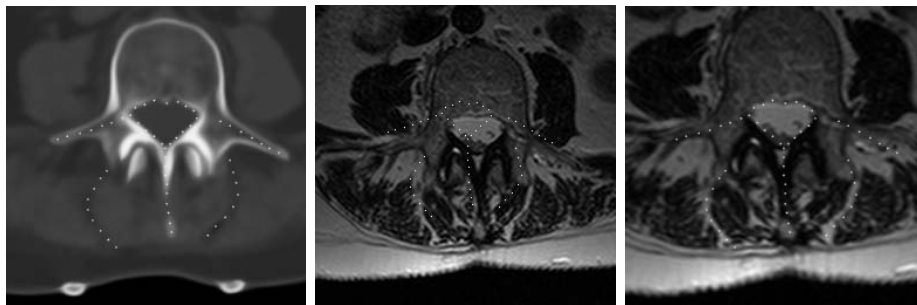


Fig. 1. Sectional morphological registration on a pair of MR and CT images of a human spine. Dotted lines mark certain features visible in the reference image. There are repeatedly drawn at the same position in the other images. The reference CT image (left), the template MR (middle) and the registered template (right) are rendered. In the middle image the misfit of structures of the CT image marked with corresponding dotted lines is clearly visible. For further details on this example we refer to [29].

As an example for the performance of the resulting algorithm the registration of real MR and CT images of a human spine has been considered (cf. Figures 1).

2.2 Matching edge sets

Now, we will consider the matching of the singular morphologies of two different images and couple this matching with edge segmentation and image denoising. In the last decade, different approaches to couple segmentation with registration have been proposed. Young and Levy [71] used segmentation results for one image to guide the search for edges in consecutive images to resolve boundaries even though they are not well defined in all images. Yezzi, Zöllei and Kapur [44] have simultaneously segmented contours in different images based on an affine matching deformation. Feron and Mohammad-Djafari [34] proposed a Bayesian approach for the joint segmentation and fusion of images via a coupling of suitable hidden Markov Models for multi modal images.

If we would minimize the Mumford-Shah functional (2) for u_T^0 and u_R^0 separately, we would obtain smooth representations u_T and u_R together with singularity sets \mathcal{S}_T and \mathcal{S}_R . Now, we sum up these two functionals and replace either the reference edge set \mathcal{S}_R by the pull back $\phi^{-1}(\mathcal{S}_T)$ of the template edge set or the template edge set \mathcal{S}_T by the push forward $\phi(\mathcal{S}_R)$ of the reference edge set. Thus, a deformation ϕ with $\mathcal{S}_R \subset \phi^{-1}(\mathcal{S}_T)$ or $\mathcal{S}_T \subset \phi(\mathcal{S}_R)$, respectively, is a suitable candidate for the minimization of the resulting combined energy. In the first case, where we use $\phi(\mathcal{S}_R)$ instead of \mathcal{S}_T , the \mathcal{H}^{d-1} measure [4] of $\phi^{-1}(\mathcal{S}_T)$ can be controlled by the \mathcal{H}^{d-1} measure of \mathcal{S}_T and the deformation ϕ , i. e., $\mathcal{H}^{d-1}(\phi(\mathcal{S}_T)) = \int_{\mathcal{S}_T} \det D\phi^{-1} |D\phi D\phi^T n_T^s \cdot n_T^s| d\mathcal{H}^{d-1}$ [25]. A similar result holds in the second case. Indeed, the control of the deformation on such lower dimensional sets is analytically and numerically difficult. Hence, we omit the corresponding energy term in our joint segmentation and registration model. Finally, in the first case of the *pull back model* the energy for the coupled Mumford-Shah segmentation in the reference and the template image is given by

$$\begin{aligned} \mathcal{E}_{\text{MS}}[u_R, u_T, \mathcal{S}_T, \phi] &= \int_{\Omega} (u_R - u_R^0)^2 d\mathcal{L} + \int_{\Omega} (u_T - u_T^0)^2 d\mathcal{L} \\ &\quad + \mu \int_{\Omega \setminus \phi^{-1}(\mathcal{S}_T)} |\nabla u_R|^2 d\mathcal{L} + \mu \int_{\Omega \setminus \mathcal{S}_T} |\nabla u_T|^2 d\mathcal{L} + \eta \mathcal{H}^{d-1}(\mathcal{S}_T) \end{aligned} \quad (21)$$

with $\mu, \eta > 0$; whereas in the second case for the *push forward model* we consider the energy

$$\begin{aligned} \mathcal{E}_{\text{MS}}[u_R, u_T, \mathcal{S}_T, \phi] &= \int_{\Omega} (u_R - u_R^0)^2 d\mathcal{L} + \int_{\Omega} (u_T - u_T^0)^2 d\mathcal{L} \\ &\quad + \mu \int_{\Omega \setminus \mathcal{S}_R} |\nabla u_R|^2 d\mathcal{L} + \mu \int_{\Omega \setminus \phi(\mathcal{S}_R)} |\nabla u_T|^2 d\mathcal{L} + \eta \mathcal{H}^{d-1}(\mathcal{S}_R). \end{aligned} \quad (22)$$

Let us remark that these energies do not care about the orientation of the normals on the singularity sets \mathcal{S}_R and $\phi(\mathcal{S}_R)$. Thus, it is invariant not only under monotone contrast changes.

A level set method In this section we will review a level set model for the coupled free discontinuity problem (22). Thereby, we restrict ourselves to edge sets which are the union of finitely many Jordan-curves. In this case, the feature set can be viewed as the boundary of detected segments, which are mapped to similar segment boundaries in the second image. For a large class of images, this is a very suitable and convenient approach, since images can often be decomposed into a finite set of independent objects. However this is not always the case. Crack tips might occur not only due to weak edge information but due to the fact that the image contains interrupted discontinuity sets (cf. the phase field approximation below).

In a shape optimization framework, we start with an initial shape describing the edge set and evolve it based on a suitable energy descent. The edge set may be elegantly described and propagated by the level set approach of OSHER and SETHIAN [58,59]. In [42] a level set based, Newton-Type regularized optimization algorithm has been derived for the minimization of the original Mumford-Shah functional. That work is the algorithmical basis for our method. For related approaches we refer to [13]. In explicit, we consider \mathcal{S}_R to be given as the zero level set of the level set function $\Xi : \Omega \rightarrow \mathbb{R}$, i. e., $\mathcal{S}_R = \{x : \Xi(x) = 0\}$.

The functional (22) depends on the variables u_R , u_T , ϕ and \mathcal{S}_R . In the process of minimization we develop different strategies for the different variables. Fortunately, the functional is quadratic with respect to the variables u_R and u_T . Hence, we may minimize (22) for fixed \mathcal{S}_R and ϕ over image spaces of u_R and u_T . Let us now denote by $u_R[\mathcal{S}_R]$ and $u_T[\mathcal{S}_R, \phi]$ the corresponding minimizers. They are obtained solving the Euler Lagrange equations with respect to u_R and u_T :

$$\begin{aligned} -\mu \Delta u_R + u_R &= u_R^0 & \text{in } \Omega \setminus \mathcal{S}_R \\ \partial_{n[\mathcal{S}_R]} u_R &= 0 & \text{on } \mathcal{S}_R, \\ -\mu \Delta u_T + u_T &= u_T^0 & \text{in } \Omega \setminus \phi[\mathcal{S}_R], \\ \partial_{n[\phi(\mathcal{S}_R)]} u_T &= 0 & \text{on } \phi(\mathcal{S}_R). \end{aligned} \tag{23}$$

It is obvious that the minimizer with respect to u_R depends only on \mathcal{S}_R , whereas the minimizer with respect to u_T depends also on ϕ via the domain of integration $\Omega \setminus \phi[\mathcal{S}_R]$. Now we can define the *reduced* functional

$$\hat{\mathcal{E}}[\mathcal{S}_R, \phi] = \mathcal{E}[u_R[\mathcal{S}_R], u_T[\mathcal{S}_R, \phi], \mathcal{S}_R, \phi] + \mathcal{E}_{elast}[\phi]. \tag{24}$$

Via an integral transform, we first decouple \mathcal{S}_R and ϕ and obtain

$$\begin{aligned} \hat{\mathcal{E}}[\mathcal{S}_R, \phi] &= \int_{\Omega} (u_R[\mathcal{S}_R] - u_R^0)^2 d\mathcal{L} + \mu \int_{\Omega \setminus \mathcal{S}_R} |\nabla u_R[\mathcal{S}_R]|^2 d\mathcal{L} \\ &+ \int_{\Omega} \left((u_T[\mathcal{S}_R, \phi] - u_T^0)^2 \circ \phi \right) |\det \mathcal{D}\phi| d\mathcal{L} \\ &+ \mu \int_{\Omega \setminus \mathcal{S}_R} \left(|\nabla u_T[\mathcal{S}_R, \phi]|^2 \circ \phi \right) |\det \mathcal{D}\phi| d\mathcal{L} + \eta \mathcal{H}^{d-1}[\mathcal{S}_R] + \mathcal{E}_{elast}[\phi]. \end{aligned}$$

Now we can apply (4), where we have to integrate along the boundaries from both sides of the contour, which leads to corresponding jump terms. We obtain

$$\begin{aligned} \partial_{\mathcal{S}_R} \hat{\mathcal{E}}[\mathcal{S}_R, \phi](\vartheta) &= \int_{\mathcal{S}_R} (\llbracket (u_R[\mathcal{S}_R] - u_R^0)^2 \rrbracket + \mu \llbracket |\nabla u_R[\mathcal{S}_R]|^2 \rrbracket) \vartheta \, d\mathcal{H}^{d-1} \\ &\quad + \int_{\mathcal{S}_R} (\llbracket (u_T[\mathcal{S}_R, \phi] - u_T^0)^2 \rrbracket + \mu \llbracket |\nabla u_T[\mathcal{S}_R, \phi]|^2 \rrbracket) \circ \phi \, |\det \mathcal{D}\phi| \vartheta \, d\mathcal{H}^{d-1} \\ &\quad + \eta \int_{\mathcal{S}_R} h \vartheta \, d\mathcal{H}^{d-1}. \end{aligned}$$

Recall that $u_R[\mathcal{S}_R]$ and $u_T[\mathcal{S}_R, \phi]$ are defined as the solutions of the corresponding elliptic boundary value problems (23). For the Fréchet derivative of $\hat{\mathcal{E}}$ with respect to the deformation ϕ in a direction ψ we obtain

$$\begin{aligned} \partial_\phi \hat{\mathcal{E}}[\phi](\psi) &= \int_{\phi[\mathcal{S}_R]} (\llbracket |u_T[\mathcal{S}_R, \phi] - u_T^0|^2 \rrbracket + \mu \llbracket |\nabla u_T[\mathcal{S}_R, \phi]|^2 \rrbracket) (\psi \circ \phi^{-1} \cdot n_{\phi[\mathcal{S}_R]}) \, d\mathcal{H}^{d-1} \\ &\quad + \partial_\phi \mathcal{E}_{\text{reg}}[\phi](\psi), \end{aligned}$$

where the transformed normal is again given by $n_{\phi[\mathcal{S}_R]} = |\text{cof } \mathcal{D}\phi n[\mathcal{S}_R]|^{-1} \text{cof } \mathcal{D}\phi n[\mathcal{S}_R]$.

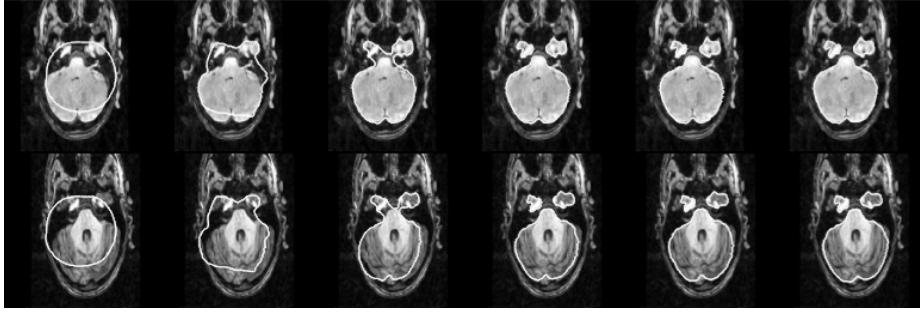


Fig. 2. For the joint segmentation approach, the evolution of level sets in a reference (top) and a template (bottom) image during the numerical energy relaxation are shown.

Hence, we have all the ingredients at hand to construct a gradient descent algorithm for this shape optimization problem. As outlined in Section 1.3 for the classical Mumford Shah model, the level set function ξ is assumed to be approximated by a finite element function Ξ in the space \mathcal{V}^h on the domain Ω . This discrete function splits the domain into two discrete domains $\Omega^+[\mathcal{S}_R]$ and $\Omega^-[\mathcal{S}_R]$. On these two domains the discrete counterparts of the equations (23) are solved via a composite finite element approach. Given the discrete solutions U_R and U_T we are then able to compute both a regularized shape gradient and a regularized gradient with respect to a discrete deformation $\Phi \in (\mathcal{V}^h)^2$ based on the above formulas for the variation of the total energy with respect to \mathcal{S}_R and ϕ . We demonstrate the performance of the resulting methods for 2D brain images. Fig. 2 shows the relaxation of level sets segmenting brain structures jointly in two images.

A phase field model Now, we suggest for the joint edge segmentation and registration problem a coupled phase field formulation. This model picks up the pull back model (21) and represents the template edge set by diffused interface described by a phase field variable v . This phase field, describing the edge set \mathcal{S}_T of the image u_T and simultaneously $v \circ \phi$, represents a super set of the edge set \mathcal{S}_R in the image u_R . The corresponding variational formulation in the spirit of the Ambrosio Tortorelli model is then given by the functional

$$\begin{aligned} \mathcal{E}_{AT}^\varepsilon[u_R, u_T, v, \phi] &:= \int_{\Omega} \left\{ (u_R - u_R^0)^2 + (u_T - u_T^0)^2 \right\} d\mathcal{L} \\ &\quad + \mu \int_{\Omega} \left\{ (v^2 \circ \phi + k_\varepsilon) |\nabla u_R|^2 + (v^2 + k_\varepsilon) |\nabla u_T|^2 \right\} d\mathcal{L} \\ &\quad + \eta \int_{\Omega} \left\{ \varepsilon |\nabla v|^2 + \frac{1}{4\varepsilon} (v-1)^2 \right\} d\mathcal{L} \end{aligned} \quad (25)$$

with $k_\varepsilon = o(\varepsilon)$. Here, the phase field function v corresponds to the contour Γ^ϕ and the contour Γ is described by $v \circ \phi$. The first integral measures the deviation of u_R and u_T to the data in the L^2 -sense. The second integral now forces the signature v^2 to be small where u_T has steep gradients and, correspondingly, $v^2 \circ \phi$ to be small where u_R has steep gradients. On the other hand, this determines ϕ to align the signature function in the reference domain to line up with the edges of u_R , and finally, for fixed signature and deformation, the smoothness of the images u_R and u_T is controlled, i. e., steep gradients of u_T are penalized where $v \not\approx 0$ and analogously for u_R .

Again, the deformation ϕ will mainly be determined along the discontinuity sets. Indeed, as outlined above, away from the contours the phase field, v will approximately be identical to 1, and hence variations of ϕ will not change the energy in these regions. Hence, we again consider a nonlinear hyperelastic regularization given by the additional energy function $\mathcal{E}_{elast}[\phi]$ (8) and finally define

$$\mathcal{E}^\varepsilon[u_R, u_T, v, \phi] := \mathcal{E}_{AT}^\varepsilon[u_R, u_T, v, \phi] + \alpha \mathcal{E}_{elast}[\phi]$$

and ask for minimizers. In what follows, let us calculate the variations of this functional with respect to the variables u_R , u_T and v in directions ζ and ϑ , respectively:

$$\begin{aligned} \partial_{u_R} \mathcal{E}_{AT}^\varepsilon[u_R, u_T, v, \phi](\zeta) &= 2 \int_{\Omega} (u_R - u_R^0) \cdot \zeta d\mathcal{L} + 2\mu \int_{\Omega} (v^2 \circ \phi + k_\varepsilon) \nabla u_R \cdot \nabla \zeta d\mathcal{L} \\ \partial_{u_T} \mathcal{E}_{AT}^\varepsilon[u_R, u_T, v, \phi](\zeta) &= 2 \int_{\Omega} (u_T - u_T^0) \cdot \zeta d\mathcal{L} + 2\mu \int_{\Omega} (v^2 + k_\varepsilon) \nabla u_T \cdot \nabla \zeta d\mathcal{L} \\ \partial_v \mathcal{E}_{AT}^\varepsilon[u_R, u_T, v, \phi](\vartheta) &= 2\mu \int_{\Omega} |\nabla u_T|^2 v \cdot \vartheta d\mathcal{L} + 2\mu \int_{\Omega} |\nabla u_R|^2 (v \circ \phi) \cdot (\vartheta \circ \phi) \\ &\quad + 2\eta \int_{\Omega} \varepsilon \nabla v \cdot \nabla \vartheta + \frac{1}{4\varepsilon} (v-1) \vartheta d\mathcal{L}. \end{aligned}$$

We rewrite this via the transformation formula:

$$\begin{aligned} \partial_v \mathcal{E}_{AT}^\varepsilon[u_R, u_T, v, \phi](\vartheta) &= 2\mu \int_{\Omega} |\nabla u_T|^2 v \cdot \vartheta d\mathcal{L} + 2\mu \int_{\Omega} |\nabla u_R|^2 \circ \phi^{-1} v \cdot \vartheta \det \mathcal{D}\phi^{-1} d\mathcal{L} \\ &\quad + 2\eta \int_{\Omega} \varepsilon \nabla v \cdot \nabla \vartheta + \frac{1}{4\varepsilon} (v-1) \vartheta d\mathcal{L}. \end{aligned}$$

Hence, for fixed v and ϕ , the reconstructed images u_R and u_T can be computed by solving the elliptic problems

$$\begin{aligned} u_R - \mu \operatorname{div} ((v^2 \circ \phi + k_\varepsilon) \nabla u_R) &= u_R^0 \\ u_T - \mu \operatorname{div} ((v^2 + k_\varepsilon) \nabla u_T) &= u_T^0 \end{aligned}$$

in Ω with boundary conditions $\partial_n u_R = \partial_n u_T = 0$ on $\partial\Omega$. Since $v \geq 0$, the corresponding bilinear-forms are coercive. Furthermore, we are able to find for each u_T , u_R and ϕ the optimal phase field v as the solution of the Euler-Lagrange equation with respect to the variation in the variable v , i. e.,

$$\mu |\nabla u_T|^2 v + \mu |\nabla u_R|^2 \circ \phi^{-1} v \det \mathcal{D}\phi^{-1} + \frac{\eta}{4\varepsilon} (v-1) - \eta \varepsilon \Delta v = 0$$

in Ω and $\partial_n v = 0$ on $\partial\Omega$. Finally, the variation of the energy with respect to the deformation in a direction ψ is given by

$$\begin{aligned} \partial_\phi \mathcal{E}_{AT}^\varepsilon[u_R, u_T, v, \phi](\psi) &= 2\mu \int_\Omega |\nabla u_R|^2 v \circ \phi (\nabla v \circ \phi \cdot \psi) \, d\mathcal{L} \\ &= 2\mu \int_\Omega |\nabla u_R|^2 \circ \phi^{-1} v (\nabla v \cdot \psi \circ \phi^{-1}) \det \mathcal{D}\phi^{-1} \, d\mathcal{L}. \end{aligned}$$

Analogously to the approach chosen in the above sharp interface model, the energy functional can be reduced to depending only on ϕ , where $u_R[\phi]$, $u_T[\phi]$ and $v[\phi]$ are determined as the unique solutions of the quadratic minimization problem for fixed deformation ϕ :

$$\hat{\mathcal{E}}^\varepsilon[\phi] = \mathcal{E}^\varepsilon[u_R[\phi], u_T[\phi], v[\phi], \phi]. \quad (26)$$

Based on these energy variations of energy we can now construct an alternating minimization algorithm for this diffusive shape optimization problem. Hence, the image intensity functions u_R , u_T , the phase field function v and the deformation ϕ are approximated by corresponding finite element functions U_R , U_T , V , and Φ in the finite element space \mathcal{V}^h and $(\mathcal{V}^h)^d$ on the domain Ω . Given the discrete solutions U_R and U_T we are then able to compute both a regularized shape gradient and a regularized gradient with respect to the deformation ϕ based on the above formulas for the variation of the total energy with respect to \mathcal{S} and ϕ . Fig. 3 depicts an application where brain structures of MR scans of two different patients with varying image contrast are to be matched. The underlying 3D images consist of 257^3 voxels and thus $3 \cdot 257^3$ unknowns in the nodal vector of deformation. Our results demonstrate that without any pre-registration the algorithm is able to generate a fairly good match. Nevertheless, due to the structural differences in the two brains the capabilities of the algorithm are locally limited basically by the built in regularity control of the elastic deformation. The algorithm applied to raw data without any preprocessing is still capable to generate a reasonable overall matching for instance of the cortex outline or of the skull. But it significantly suffers from the local deviation of medical morphology which requires prior knowledge on non local anatomy from the underlying mathematical morphology with its purely local definition.

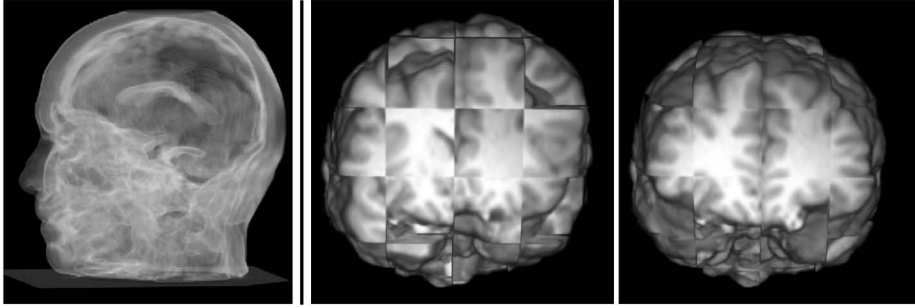


Fig. 3. On the left, the 3D phase field corresponding to an MR image is shown. Furthermore, the matching of two MR brain images of different patients is depicted. We use a volume renderer based on ray casting (VTK) for a 3D checkerboard with alternating boxes of the reference and the pull back of the template image to show the initial mismatch of MR brain images of two different patients (middle) and the results of our matching algorithm (right).

2.3 Matching singular and regular morphology

Now, we also have all the ingredients at hand to formulate the variational problem for a matching of the singular and regular image morphology combined with a simultaneous edge segmentation and denoising in the template and the reference image. We collect the matching energy (22) for the singular morphology, the matching energy (13) for the regular morphology, the elastic regularization energy (8) and define the global energy

$$\mathcal{E}[u_R, u_T, \mathcal{S}_T, \phi] := \mathcal{E}_{MS}[u_R, u_T, \mathcal{S}_T, \phi] + \mathcal{E}_{GM}[u_R, u_T, \phi] + \mathcal{E}_{reg}[\phi]. \quad (27)$$

Even for very simple image pairs u_R^0 and u_T^0 we expect the resulting energy landscape to be very complicated. To address this issue, we will not restrict to a single fine scale problem but as above consider an embedding into a scale of problems to be solved from coarse to fine. This scale will be induced by the phase field approximation of the energy \mathcal{E}_{MS} . The width of the edge regions indicated by small values of v is expected to be proportional to ε . For decreasing ε we will obtain successively sharper regularized images u_T and u_R . This implicitly introduces a scale in the energy \mathcal{E}_{GM} as well. In explicit the gradients ∇u_T and ∇u_R corresponding to u_T and u_R are expected to be smoother for larger ε . Thus, we no longer have to distinguish regular and singular gradients. To focus only on the regular morphology in this energy contribution - in particular not measuring edges - we mask out a gradient comparison in the vicinity of edges. Therefore, the integrand is multiplied by $v^2 \circ \phi$ and we obtain

$$\mathcal{E}_{GM}^\varepsilon[u_T, u_R, v, \phi] = \int_{\Omega} v^2 \circ \phi g_0(\nabla u_T \circ \phi, \nabla u_R, \text{cof } \mathcal{D}\phi) d\mathcal{L}. \quad (28)$$

Finally, gathering this energy and the energy contributions from (25) and (8) we define a scale of global approximate energies

$$\mathcal{E}^\varepsilon[u_R, u_T, v, \phi] := \mathcal{E}_{AT}^\varepsilon[u_R, u_T, v, \phi] + \mathcal{E}_{GM}^\varepsilon[u_R, u_T, v, \phi] + \mathcal{E}_{reg}[\phi]$$

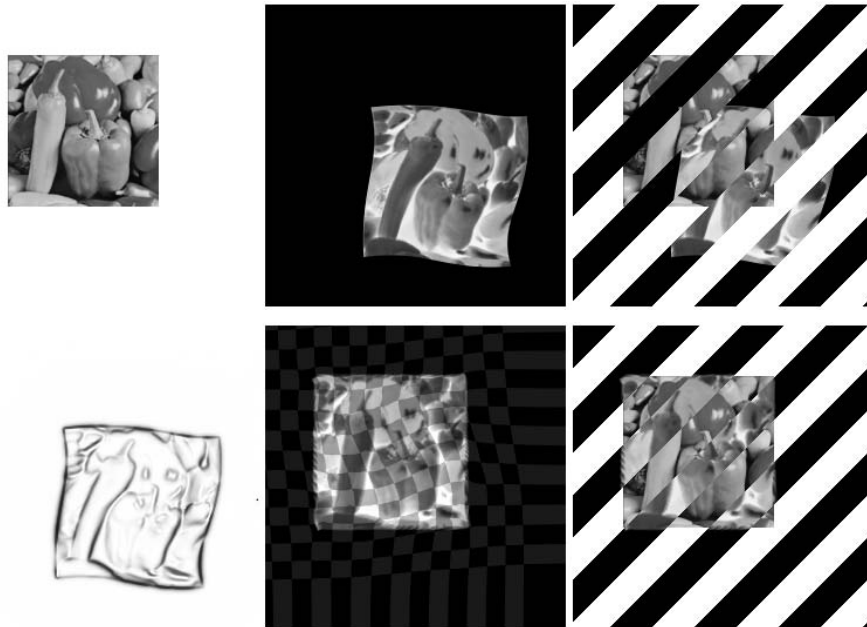


Fig. 4. A contrast invariant matching is shown. In the first row we have inverted, moved and distorted the peppers image (left) to obtain a template image (middle). On the right the initial misfit is shown. The registration result for this input data are depicted in the second row. The final phase field function v is depicted on the left. The image in the middle shows a plot of the deformation due to a relaxation of the combined energy, i. e., the registration of discontinuity sets and level sets. On the right alternating slices of the reference and the pulled back template image allow a visual validation of the matching result.

depending on the scale parameter ε . We refer to Fig. 4 for results achieved via a relaxation of this energy. Apart from \mathcal{E}_{GM} the energy depends quadratically on u_T , u_R and v . Thus, the corresponding necessary conditions to be fulfilled by a minimizer, i. e., the Euler Lagrange equations with respect to these variables, turn into linear problems. In the relaxation scheme for the deformation, which actually describes the image matching, we treat u_T , u_R and v in a quasi stationary way. In fact, the iterative relaxation proceeds as follows: For given images and deformation, we optimize w.r.t. the phase field v . In a next step, we then optimize for the regularized images u_T and u_R for given ϕ and already optimized v . Finally, we consider one gradient descent step for the global energy w.r.t. the deformation. Here, we pick up a regularized gradient descent as described above. This procedure is repeated until convergence. In the current implementation we neglect the impact of the ongoing segmentation process on the variation of the energy concerned with the regular morphology and consider the following simplification in the

method:

$$(u_T, u_R) = \arg \min_{u_T, u_R} \mathcal{E}_{AT}^E[u_T, u_R, v, \phi].$$

Even though we no longer actually minimize the global energy, the proposed restricted energy relaxation already leads to satisfying edge segmentation and matching results.

We have applied our method also to 3D medical image registration problems and present here some results, where we concentrate on a matching only of the singular morphology. In particular in 3D a cascadic multiscale approach turned out to be indispensable to ensure an efficient numerical implementation.

Finally, we demonstrate the applicability of the method by registering two different facial texture maps. Figure 5 depicts the input data, whereas Figure 6 pinpoints the differences of the different matching approaches. As in the previous example, Figure 7 illustrates the energetic improvement due to the interplay of the deformation and the phase field function, reducing the length of the overall interface by alignment of edges.



Fig. 5. A facial texture matching problem. Initial reference texture map u_R (left), initial template u_T (middle) and the initial misfit plot on the (right).

2.4 A parametric approach to surface matching

Establishing a correspondence between two surfaces is a basic ingredient in many geometry processing applications. Motivated by the ability to scan geometry with high fidelity, a number of approaches have been developed in the graphics literature to bring such scans into correspondence. Early work used parameterizations of the meshes over a common parameter domain to establish a direct correspondence between them [48]. Typically these methods are driven by user-supplied feature correspondences which are then used to drive a mutual parametrization. The main difficulty is the proper alignment of selected features during the parameterizations process [47,60,65] and the algorithmic issues associated with the management of irregular meshes and their effective overlay. Here, we address this problem on the background of deformations of elastic shells. Recently, Gu and Vemuri [38] considered matches of topological spheres through conformal maps with applications to brain matching. Their energy measures the defect of

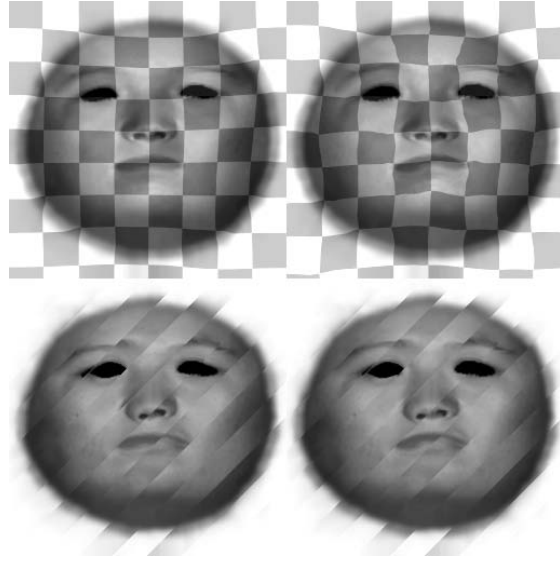


Fig. 6. Results for the facial texture matching problem given in 5. The top row shows the deformed template that has been overlaid by a uniform checkerboard pattern. On the left the regular morphology has not been taken into account, hence, mainly the face outline and strong edges are matched properly. Considering the entire energy functional significantly improves the result (right). The deformation is characterized by a much higher variability. The bottom row displays with alternating stripes the corresponding reference and pulled back template images to enable a validation of the matching results.

the conformal factor and — similar to our approach — the defect of the mean curvature. However they do not measure the correspondence of feature sets or tangential distortion, and thus do not involve a regularization energy for the ill-posed energy minimization. Furthermore, they seek a one-to-one correspondence, whereas we must address the difficult problem of partial correspondences between surfaces with boundaries.

Instead of matching two surfaces directly in 3D, we apply well-established matching methods from *image processing* in the parameter domains of the surfaces. A matching energy is introduced that can depend on curvature, feature demarcations or surface textures, and a regularization energy controls length and area changes in the induced non-rigid deformation between the two surfaces. The metric on both surfaces is properly incorporated into the formulation of the energy. This approach reduces all computations to the 2D setting while accounting for the original geometries. Consequently a fast multiresolution numerical algorithm for regular image grids can be used to solve the global optimization problem. The final algorithm is robust, generically much simpler than direct matching methods, and very fast for highly resolved triangle meshes.

Our goal is to correlate two surface patches, \mathcal{S}_A and \mathcal{S}_B , through a non-rigid spatial deformation

$$\phi_{\mathcal{S}} : \mathcal{S}_A \rightarrow \mathbb{R}^3$$



Fig. 7. The phase field v corresponding to the matching results in Figure 5. LEFT: Initial phase field. RIGHT: Phase field after alignment.

such that corresponding regions of \mathcal{S}_A are mapped onto regions of \mathcal{S}_B . In doing so, we want to avoid the general difficulty of formulating these maps directly in \mathbb{R}^3 and the particularly tedious algorithmic issues in the application, where the two surface patches are given as distinct, arbitrary triangulations. Instead, we match parameter domains covered with geometric and user-defined feature characteristics. The main benefit of this approach is that it simplifies the problem of finding correspondences for surfaces embedded in \mathbb{R}^3 to a matching problem for images in two dimensions. To ensure that the actual geometry of the surface patches is treated properly here, the energy on the deformations from one parameter space to the other will measure:

- *Elastic distortion energy*: smoothness of the deformation in terms of tangential distortion,
- *Bending energy*: bending of normals through the proper correspondence of curvature, and
- *Feature energy*: the proper correspondence of important surface and texture features.

Furthermore, it will consistently take into account the proper metrics on the parameter domains, which ensures that we are actually treating a deformation from one surface onto the other even though all computations are performed in 2D.

Physical motivation Consider the first surface to be a thin shell which we press into a mould of the second surface (cf. Figure 8). One can distinguish between stresses induced by stretching and compression and stressed induced by bending that occurs in the surface as it is being pressed. Thus ϕ_S can be regarded as the deformation of such a thin shell. We assume this deformation to be elastic. The regularization energy in Eq. (29) will measure the induced in-plane stresses, and the concrete energy density in Eq. (30) allows control over length and area-distortion in this surface-to-surface deformation. Since we are aiming for a proper correspondence of shape, we will incorporate the bending of normals in our energy with Eq. (31). Finally, the matching of feature sets in Eq. (32) will provide user-specified landmarks to guide the surface deformation. In what follows, we will develop the variational approach step-by-step.

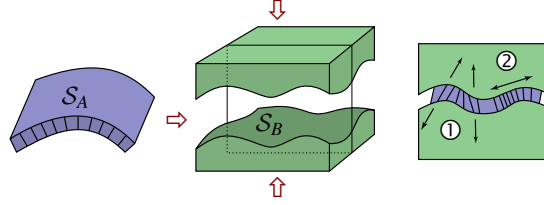


Fig. 8. A physical interpretation of ϕ_M as pressing a thin shell \mathcal{S}_A into a mould of the surface \mathcal{S}_B being matched. The bending (1) and stretching (2) of the thin shell is measured in our matching energy and minimized by the optimal match ϕ_S .

To begin with, let us set up proper parameterizations. A parameterization is a mapping from the plane onto a given surface, or in the case of its inverse, from the surface onto the plane. Consider a smooth surface $\mathcal{S} \subset \mathbb{R}^3$, and suppose $x : \omega \rightarrow \mathcal{S}$ is a parameterizations of \mathcal{S} on a parameter domain ω . For a parameterizations to be properly defined, its inverse x^{-1} cannot allow the surface to fold onto itself in the plane. In this case x is a bijection and a metric g is properly defined on ω ,

$$g = \mathcal{D}x^T \mathcal{D}x$$

where $\mathcal{D}x \in \mathbb{R}^{3,2}$ is the Jacobian of the parameterization x . The metric g acts on tangent vectors v, w on the parameter domain ω with $(gv) \cdot w = \mathcal{D}xv \cdot \mathcal{D}xw$, which is simply the inner product of tangent vectors $\mathcal{D}xv, \mathcal{D}xw$ on the surface. Thus, it follows that the metric describes how length, area and angles are distorted under the parametrization function.

Let us now focus on the distortion from the surface \mathcal{S} onto the parameter domain ω under the inverse parametrization x^{-1} . This distortion is measured by the inverse metric $g^{-1} \in \mathbb{R}^{2,2}$. Just as $\sqrt{\text{tr}(A^T A)}$ measures the average *change of length* under a linear mapping A , $\sqrt{\text{tr} g^{-1}}$ measures the average change of length of tangent vectors under the mapping from the surface onto the parameter plane. Additionally, $\sqrt{\det g^{-1}}$ measures the corresponding *change of area*. We will use these quantities in the following sections to account for the distortion of length and area on the surface as we formulate our matching energy in the parameter domain.

Measuring Distortion via a Deformation The above discussion now applies to the parameter maps x_A and x_B of the surfaces \mathcal{S}_A and \mathcal{S}_B . We suppose that these parameterizations are defined in an initial step and we assume that x_A and x_B as well as the corresponding parameter domains ω_A and ω_B are fixed from now on. Their metrics are denoted by g_A and g_B , respectively. We will now study the distortion which arises from a deformation of the first parameter domain onto the second parameter domain. First, let us consider deformations $\phi : \omega_A \rightarrow \omega_B$ which are one-to-one. This deformation between parameter domains induces a deformation between the surface patches $\phi_S : \mathcal{S}_A \rightarrow \mathcal{S}_B$ defined by

$$\phi_S := x_B \circ \phi \circ x_A^{-1}.$$

Let us emphasize that we do not actually expect a one-to-one correspondence between surface patches. Later we will relax this assumption and in particular allow for deformations ϕ with $\phi(\omega_A) \not\subset \omega_B$. The complete mapping is illustrated in Figure 9.

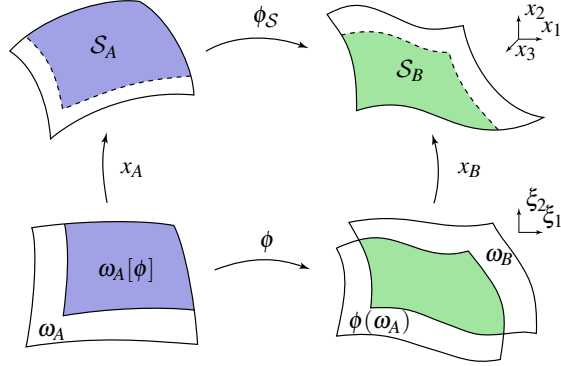


Fig. 9. The matching function $\phi_S := x_B \circ \phi \circ x_A^{-1}$ is a mapping between the corresponding shaded regions of the two surfaces. The partial correspondence is defined on $\omega_A[\phi] := \omega_A \cap \phi^{-1}(\omega_B)$.

Now let us focus on the distortion from the surface \mathcal{S}_A onto the surface \mathcal{S}_B . In elasticity, the distortion under an elastic deformation ϕ is measured by the Cauchy-Green strain tensor $\mathcal{D}\phi^T \mathcal{D}\phi$. We wish to adapt this definition to measure distortion between tangent vectors on the two surfaces, as we did with the metric g in the previous section. Therefore, we properly incorporate the metrics g_A and g_B at the deformed position and obtain the distortion tensor $\mathcal{G}[\phi] \in \mathbb{R}^{2,2}$ given by

$$\mathcal{G}[\phi] = g_A^{-1} \mathcal{D}\phi^T (g_B \circ \phi) \mathcal{D}\phi,$$

which acts on tangent vectors on the parameter domain ω_A , where where products are given in matrix notation. Mathematically, this tensor is defined implicitly via the identity $(g_A \mathcal{G}[\phi] v) \cdot w = (g_B \circ \phi) \mathcal{D}\phi v \cdot \mathcal{D}\phi w$ for tangent vectors v, w on the surface \mathcal{S}_A and their images as tangent vectors $\mathcal{D}\phi v, \mathcal{D}\phi w$ on \mathcal{S}_B , where here we have identified tangent vectors on the surfaces with vectors in the parameter domains.

As in the parametrization case, one observes that $\text{tr} \mathcal{G}[\phi]$ measures the average *change of length* of tangent vectors from \mathcal{S}_A when being mapped to tangent vectors on \mathcal{S}_B , and $\sqrt{\det \mathcal{G}[\phi]}$ measures the *change of area* under the deformation ϕ_S . Thus $\text{tr} \mathcal{G}[\phi]$ and $\sqrt{\det \mathcal{G}[\phi]}$ are natural variables for an energy density in a variational approach measuring the *regularity* of a surface deformation,

$$\mathcal{E}_{\text{elast}}[\phi] = \int_{\omega_A} W(\text{tr} \mathcal{G}[\phi], \sqrt{\det \mathcal{G}[\phi]}) \sqrt{\det g_A} d\xi. \quad (29)$$

This simple class of energy functionals was rigorously derived in [22] from a set of natural axioms for measuring the distortion of a single parametrization. In particular, the following energy density

$$W(I_1, I_2) = \alpha_l I_1 + \alpha_a (I_2^2 + (1 + \frac{\alpha_l}{\alpha_a}) I_2^{-2}) \quad (30)$$

accounts for length distortion with $I_1 = \text{tr} \mathcal{G}[\phi]$, area expansion with $I_2 = \sqrt{\det \mathcal{G}[\phi]}$ and area compression with I_2^{-1} . The weights $\alpha_l, \alpha_a > 0$ are typically chosen by the user according to the relative importance of length and area distortion.

Measuring Bending in a Deformation When we press a given surface \mathcal{S}_A into the thin mould of the surface \mathcal{S}_B , a major source of stress results from the bending of normals. We assume these stresses to be elastic as well and to depend on changes in normal variations under the deformation. Variations of normals are represented in the metric by the shape operator. For the derivation of the shape operators S_A and S_B of the surface patches \mathcal{S}_A and \mathcal{S}_B we refer to [49], where we end up with $\text{tr}(S_B \circ \phi) - \text{tr}(S_A)$ as a *measure for the bending of normals*. Since the trace of the shape operator is the mean curvature, we can instead aim to compare the mean curvature $h_B = \text{tr}(S_B)$ of the surface \mathcal{S}_B at the deformed position $\phi_S(x)$ and the mean curvature $h_A = \text{tr}(S_A)$ of the surface \mathcal{S}_A . A similar observation was used by [32] to define a bending energy for discrete thin shells. This proposed simplification neglects any rotation of directions due to the deformation, *e.g.* if the deformation aligns a curve with positive curvature on the first surface to a curve with negative curvature on the second surface and vice versa, an energy depending solely on $h_B \circ \phi - h_A$ does not recognize this mismatch. Nevertheless, in practice the bending energy

$$\mathcal{E}_{bend}[\phi] = \int_{\omega_A} (h_B \circ \phi - h_A)^2 \sqrt{\det g_A} d\xi \quad (31)$$

turns out to be effective and sufficient. By minimizing this energy, we ensure that the deformation properly matches mean curvature on the surfaces.

Matching Features Frequently, surfaces are characterized by similar geometric or texture features, which should be matched properly as well. Therefore we will incorporate a correspondence between one-dimensional feature sets in our variational approach to match characteristic lines drawn on the surface. In particular, we prefer feature lines to points for the flexibility afforded to the user, as well as to avoid the theoretical problems introduced by point constraints [19]. We will denote the feature sets by $\mathcal{F}_{\mathcal{S}_A} \subset \mathcal{S}_A$ and $\mathcal{F}_{\mathcal{S}_B} \subset \mathcal{S}_B$ on the respective surfaces. Furthermore, let $\mathcal{F}_A \subset \omega_A$ and $\mathcal{F}_B \subset \omega_B$ be the corresponding sets on the parameter domains. We are aiming for a proper match of these sets via the deformation, *i.e.*

$$\phi_S(\mathcal{F}_{\mathcal{S}_A}) = \mathcal{F}_{\mathcal{S}_B}$$

or in terms of differences, $\mathcal{F}_{\mathcal{S}_A} \setminus \phi_S^{-1}(\mathcal{F}_{\mathcal{S}_B}) = \emptyset$ and $\mathcal{F}_{\mathcal{S}_B} \setminus \phi_S(\mathcal{F}_{\mathcal{S}_A}) = \emptyset$. A rigorous way to reflect this in our variational approach is with a third energy contribution,

$$\mathcal{E}_{\mathcal{F}}[\phi] = \mathcal{H}^1(\mathcal{F}_{\mathcal{S}_A} \setminus \phi_S^{-1}(\mathcal{F}_{\mathcal{S}_B})) + \mathcal{H}^1(\mathcal{F}_{\mathcal{S}_B} \setminus \phi_S(\mathcal{F}_{\mathcal{S}_A})) \quad (32)$$

where $\mathcal{H}^1(\mathcal{A})$ is the one-dimensional Hausdorff measure of a set \mathcal{A} on the corresponding surface. Roughly speaking, this gives a symmetric measurement of the size of the

mismatch of the features. This type of energy does not lend itself to a robust numerical minimization. Therefore, we will instead consider a suitable approximation of Eq. (32) that involves the *distance on the surface to the feature sets* and define

$$\begin{aligned} \tilde{\mathcal{E}}_{\mathcal{F}}^{\varepsilon}[\phi] = & \int_{\omega_A} (\eta^{\varepsilon} \circ d_A(\xi)) (\vartheta^{\varepsilon} \circ d_B(\phi(\xi))) \sqrt{\det g_A} d\xi + \\ & \int_{\omega_B} (\eta^{\varepsilon} \circ d_B(\xi)) (\vartheta^{\varepsilon} \circ d_A(\phi^{-1}(\xi))) \sqrt{\det g_B} d\xi \end{aligned} \quad (33)$$

where $d_A(\cdot) = \text{dist}_A(\cdot, \mathcal{A})$ and $d_B(\cdot) = \text{dist}_B(\cdot, \mathcal{A})$ are distance functions on the parameter domains ω_A and ω_B with respect to some set \mathcal{A} on the corresponding surface. Note that we measure distance either in the metric g_A on ω_A or in the metric g_B on ω_B . Additionally, we define the localization functions

$$\eta^{\varepsilon}(s) = \frac{1}{\varepsilon} \max\left(1 - \frac{s}{\varepsilon}, 0\right), \quad \vartheta^{\varepsilon}(s) = \min\left(\frac{s^2}{\varepsilon}, 1\right)$$

which act as cut-off functions. For Lipschitz continuous feature sets and bi-Lipschitz continuous deformations, we observe that $\tilde{\mathcal{E}}_{\mathcal{F}}^{\varepsilon}[\phi] \rightarrow \mathcal{E}_{\mathcal{F}}[\phi]$ as $\varepsilon \rightarrow 0$, which motivates our approximation. In view of the later discretization, we can reformulate the second term in Eq. (33) as

$$\int_{\omega_A} (\eta^{\varepsilon} \circ d_B(\phi(\xi))) (\vartheta^{\varepsilon} \circ d_A(\xi)) \sqrt{\det g_B(\phi(\xi))} \det \mathcal{D}\phi d\xi.$$

Usually, we cannot expect that $\phi_S(\mathcal{S}_A) = \mathcal{S}_B$, particularly near the boundary where certain subregions of \mathcal{S}_A will have no corresponding counterpart on \mathcal{S}_B and vice versa. Therefore, we must allow for points on \mathcal{S}_B with no pre-image in \mathcal{S}_A under a matching deformation ϕ_S and points on \mathcal{S}_A which are not correlated to points on \mathcal{S}_B via ϕ_S (cf. Figure 9). Thus we must adapt the variational formulation accordingly. If $\phi(\omega_A) \neq \omega_B$, then ϕ_S is now defined on $x_A(\omega_A[\phi])$ only, where

$$\omega_A[\phi] := \phi^{-1}(\phi(\omega_A) \cap \omega_B)$$

is the corresponding subset of the parameter domain ω_A . Furthermore, we define new energies (with modifications marked in red):

$$\begin{aligned} \mathcal{E}_{bend}[\phi] &= \int_{\omega_A[\phi]} (h_B \circ \phi - h_A)^2 \sqrt{\det g_A} d\xi, \\ \mathcal{E}_{\mathcal{F}}[\phi] &= \mathcal{H}^1(\omega_A[\phi] \cap \mathcal{F}_{\mathcal{S}_A} \setminus \phi_S^{-1}(\mathcal{F}_{\mathcal{S}_B})) + \\ &\quad \mathcal{H}^1(\mathcal{F}_{\mathcal{S}_B} \setminus \phi_S(\omega_A[\phi] \cap \mathcal{F}_{\mathcal{S}_A})). \end{aligned}$$

For an energy that controls tangential distortion, it is still helpful to control the regularity of the deformation outside the actual matching domain $\omega_A[\phi]$, where we would like to allow significantly larger deformations by using a “softer” elastic material. Hence we will suppose that g_B , which is initially only defined on ω_B , is extended to \mathbb{R}^2 and takes values that are relatively small to allow for greater stretching.

In the minimization algorithm, we need descent directions which will involve derivatives of these energies with respect to the deformation ϕ . In taking these derivatives,

integrals over the variable boundary $\partial\omega_A[\phi]$ will appear. Since these are tedious to treat numerically, we will rely on another approximation for the sake of simplicity. Our strategy here is to change the domain of integration $\omega_A[\phi]$ to a superset ω which extends beyond the boundary $\partial\omega_A[\phi]$. Doing so means that special treatment of boundary integrals is no longer necessary, although we are now required to evaluate the integrands of the energies outside of ω_A , and similarly for deformed positions outside of ω_B . To achieve this, we will extend our surface quantities onto $\omega \setminus \omega_A$ and $\omega \setminus \omega_B$, respectively, by applying a harmonic extension with natural boundary conditions on $\partial\omega$ to g_A, g_B and h_A, h_B (e.g., we define h_A as the solution of Laplace's equation on $\omega \setminus \omega_A$ with vanishing flux on $\partial\omega$). Additionally, we introduce a regularized characteristic function

$$\chi_{\mathcal{A}}^\varepsilon(\xi) = \max(1 - \varepsilon^{-1} \text{dist}(\xi, \mathcal{A}), 0)$$

to cause the energy contributions to be ignored at some distance ε away from $\omega_A[\phi]$. Thus, instead of dealing with a deformation dependent domain $\omega[\phi]$ in the definition of our different energy contributions, we always integrate over the *whole* image domain ω and insert the product of the two regularized characteristic functions

$$\chi^\varepsilon(\xi) = \chi_{\omega_A}^\varepsilon(\xi) \chi_{\omega_B}^\varepsilon(\phi(\xi))$$

as an additional factor in the energy integrand. We apply this modification to the energy \mathcal{E}_{bend} (31) and the already regularized energy $\tilde{\mathcal{E}}_{\mathcal{F}}^\varepsilon$ (33) and denote the resulting energies by $\mathcal{E}_{bend}^\varepsilon$ and $\mathcal{E}_{\mathcal{F}}^\varepsilon$, respectively. Furthermore, for the elastic energy $\mathcal{E}_{elast}[\phi]$ we assume a very soft elastic material outside $\omega_A[\phi]$ and the actual material parameters inside this partial matching domain. Hence, as an approximate model we consider

$$\mathcal{E}_{elast}^{\varepsilon, \delta}[\phi] = \int_{\omega_A} (\delta + (1 - \delta)\chi^\varepsilon(\xi)) W(\text{tr}\mathcal{G}[\phi], \sqrt{\det\mathcal{G}[\phi]}) \sqrt{\det g_A} d\xi$$

for some fixed, small δ .

Definition of the matching energy We are now ready to collect the different cost functionals and define the global matching energy. Depending on the user's preference, we introduce weights $\beta_{bend}, \beta_{elast}, \beta_{\mathcal{F}}$ for the energies $\mathcal{E}_{bend}^\varepsilon, \mathcal{E}_{elast}$ and $\mathcal{E}_{\mathcal{F}}^\varepsilon$, respectively, and define the global energy

$$\mathcal{E}^\varepsilon[\phi] = \beta_{bend} \mathcal{E}_{bend}^\varepsilon[\phi] + \beta_{elast} \mathcal{E}_{elast}^{\varepsilon, \delta}[\phi] + \beta_{\mathcal{F}} \mathcal{E}_{\mathcal{F}}^\varepsilon[\phi]$$

which measures the quality of a matching deformation ϕ on the domain ω . In the limit for $\varepsilon, \delta \rightarrow 0$ we aim at an approximation of the energy $\mathcal{E}[\phi] = \beta_{bend} \mathcal{E}_{bend}[\phi] + \beta_{elast} \mathcal{E}_{elast}[\phi] + \beta_{\mathcal{F}} \mathcal{E}_{\mathcal{F}}[\phi]$. Figure 10 demonstrates the capability of the presented approach to describe a partial matching problem in variational form. Based on the matching we can generate warps between different surface based on a linear blend between matched points on the different geometries (cf. Figures 11 and 12). The figure 13 shows the distortion of a checkerboard pattern on the parameter domain and the corresponding distortion on the surface.

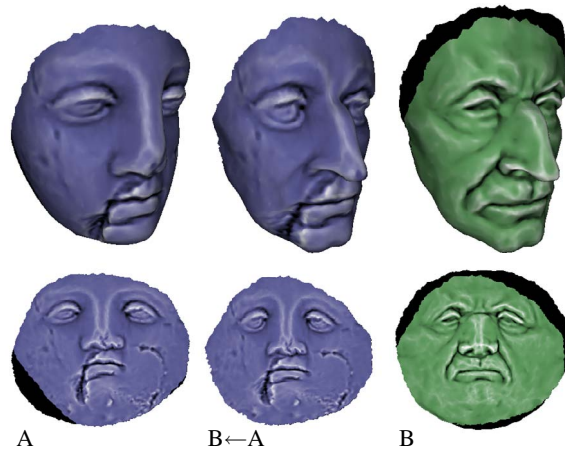


Fig. 10. For surfaces with boundaries, a partial correspondence is often desired. The correspondence is defined where their parameter domains intersect under the matching deformation (bottom). In this domain, quantities such as texture maps can be mapped between the surfaces (center). The unmatched regions are in black.



Fig. 11. A morphing between two different faces is shown.

3 Joint motion estimation, restoration, and deblurring

In this section we introduce a variational method which jointly handles motion estimation, moving object detection and motion blur deconvolution (cf. Fig. 17). The proposed framework is again a Mumford-Shah type variational formulation, which includes an explicit modeling of the motion-blur process as well as shape and image regularization terms. The input to the variational formulation are two consecutive frames, while the

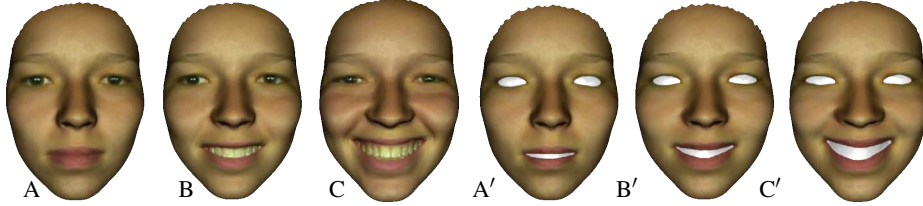


Fig. 12. Morphing through keyframe poses A, B, C is accomplished through pair-wise matches $A \rightarrow B$ and $B \rightarrow C$. Starting with A we blend its shape into B using $A \rightarrow B$, and then morph to C by applying $A \rightarrow B$ followed by $B \rightarrow C$. The skin texture from A is used throughout. Because of the close similarity in the poses, one can expect the intermediate blends A', B', C' to correspond very well with the original keyframes A, B, C , respectively.

output are the corresponding reconstructed frames, the segmented moving object, and the actual motion velocity. As in the problems discussed so far the joint estimation of motion, moving object region and reconstructed images outperforms techniques where each individual unknown is individually handled.

3.1 The motion blur model

Images from an image sequence captured with a video camera are integrated measurements of light intensity emitted from moving objects over the aperture time interval of the camera. Let $u : [-T, T] \times \Omega; (t, x) \mapsto \mathbb{R}$ denote a continuous sequence of scene intensities over a time interval $[-T, T]$ and on a spatial image domain Ω observed via the camera lens. The video sequence recorded with the camera consists of a set of images $g_i : \Omega \rightarrow \mathbb{R}$ associated with times t_i , for $i = 1, \dots, m$, given as the convolution

$$g_i(x) = \frac{1}{\tau} \int_{t_i - \frac{1}{2}\tau}^{t_i + \frac{1}{2}\tau} u(t + s, x) ds \quad (34)$$

over the aperture time τ . For the time integral, we propose a box filter, which realistically approximates the mechanical shutters of film cameras and the electronic read out of modern CCD video recorders. In the simplest case, where the sequence f renders an object moving at constant velocity $w \in \mathbb{R}^2$, i.e. $u(x - sw) = u(t + s, x)$, we can transform integration in time to an integration in space and obtain for the recorded images

$$g_i(x) = \frac{1}{\tau} \int_{-\frac{1}{2}\tau}^{\frac{1}{2}\tau} u(x - sw) ds = (u * h_w)(x), \quad (35)$$

for a one dimensional filter kernel $h_w = \delta_0(\frac{w^\perp}{|w|} \cdot y)h(\frac{w}{|w|} \cdot y)$ with filter width $\tau|w|$ in the direction of the motion trajectory $\{y = x + sw : s \in \mathbb{R}\}$. Here w^\perp denotes w rotated

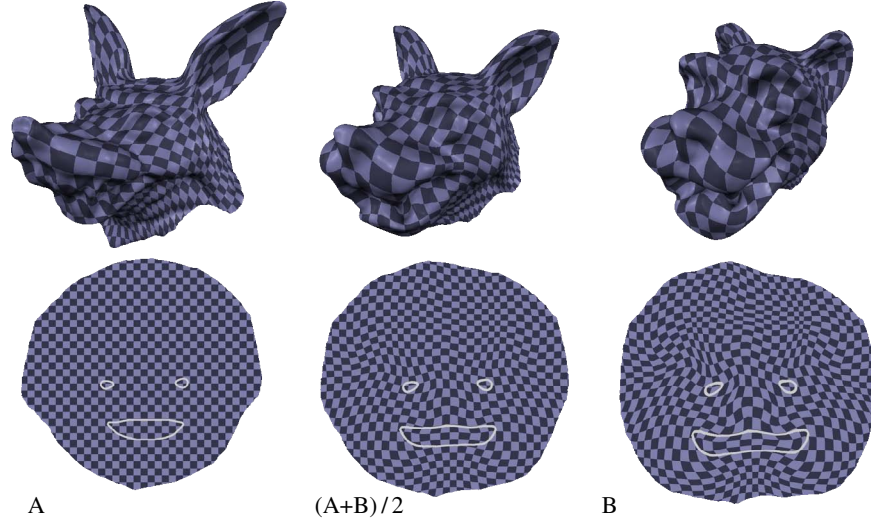


Fig. 13. Large deformations are often needed to match surfaces that have very different shapes. A checkerboard is texture mapped onto the first surface as it morphs to the second surface (top). The matching deformation shown in the parameter domain (bottom) is smooth and regular, even where the distortion is high (*e.g.*, around the outlines of the mouth and eyes).

by 90 degrees, δ_0 is the usual 1D Dirac distribution and h the 1D block filter with $h(s) = \frac{1}{\tau|w|}$ for $s \in [-\frac{\tau|w|}{2}, \frac{\tau|w|}{2}]$ and $h(s) = 0$, else. In case of an object moving in front of a (still) background the situation is somewhat more complicated. At a point x close to the boundary of the object, the convolution (34) decomposes into a spatial convolution of object intensities along the motion path for the sub-interval of the aperture interval where the object covers the background at position x , and a retrieval of the background intensity for the remaining opening time of the lens. Figure 14 shows a comparison between the actually observed motion blur and results obtained by a (wrongly) direct application of the spatial convolution formula (35) on a moving circular object in front of a textured background (more specifics on this below). This observation is particularly important for the reliable recovery of boundaries of moving objects from recorded video frames g_i and subsequently for the proper restoration of image frames (cf. Fig. 15 for a corresponding comparison).

In what follows we consider an object moving with speed $w \in \mathbb{R}^2$ in front of a still background $u_{bg} : \Omega \rightarrow \mathbb{R}$. The object at time 0 is represented by an intensity function $u_{obj} : \mathcal{O} \rightarrow \mathbb{R}$ defined on an object domain \mathcal{O} . From u_{obj} and u_{bg} one assembles the actual scene intensity function

$$u(t, x) = u_{obj}(x - tw)\chi_{obj}(x - wt)u_{bg}(x)(1 - \chi_{obj}(x - wt)) \quad (36)$$

at time t , where $\chi_{obj} : \mathbb{R}^2 \rightarrow \mathbb{R}$ denotes the characteristic function of \mathcal{O} . Now, inserting (36) in (34) and then using (35) on \mathcal{O} , we deduce the correct formula for the theoretic-

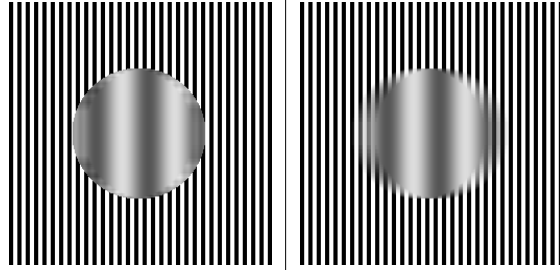


Fig. 14. We consider a moving circle with back and white stripes in front of a similarly textured background. For this test case a comparison is shown between the wrong (left) motion blur model which ignores the motion discontinuity at the boundary and our realistic, consistent model (right) given in (36) .

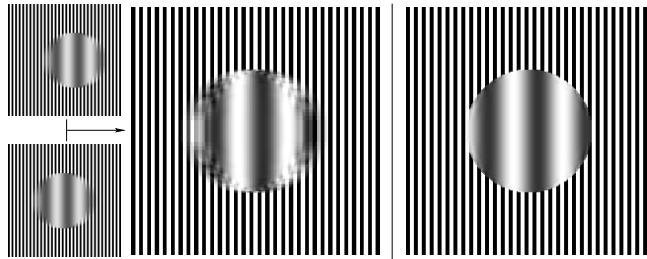


Fig. 15. Given two frames for the realistic motion blur showing the moving circle on the texture background from Fig. 14 (left), computational results for the deblurring are depicted based on the wrong motion blur model built into G_i (middle), and on our consistent model (right). This clearly outlines the importance of a proper handling of the motion discontinuity in the considered motion blur model.

cally observed motion blur at time t_i ,

$$G_i[\mathcal{O}, w, u_{\text{obj}}, u_{\text{bg}}](x) = ((u_{\text{obj}}\chi_{\text{obj}}) * h_w)(x - t_i w) + u_{\text{bg}}(x)(1 - (\chi_{\text{obj}} * h_w)(x - t_i w)),$$

for given object domain \mathcal{O} , motion velocity w , and object and image (background) intensity functions u_{obj} and u_{bg} respectively. If we do not carefully model the observed intensities while the moving object occludes and uncovers the background, we would observe $(u_{\text{obj}}(t, \cdot) * h_w)$ on the object domain and u_{bg} elsewhere (cf. the combination of Eq. (14) and Eq. (3) in [33]). Given the more precise motion blur model proposed here, we now proceed to derive a variational formulation to simultaneously estimate all parameters in this equation based on two consecutive frames.

3.2 Joint variational approach

Given two frames g_1 and g_2 of a video sequence with motion blur recorded at times t_1 and t_2 , respectively, we construct a variational model to extract from these frames the domain \mathcal{O} , the image intensity u_{obj} of a moving object and the motion velocity w . Here, we propose that the background intensity u_{bg} can a priori be extracted from the video sequence, for example, by averaging pixels with stable values over a sequence of frames. We aim at formulating a joint energy for these degrees of freedom. Modeling this energy we take into account the following observations:

Given w and intensity maps $u_{\text{obj}}, u_{\text{bg}} : \Omega \rightarrow \mathbb{R}$ (extended on the whole domain in a suitable way), we phrase the identification problem of the object boundary $\mathcal{S} = \partial\mathcal{O}$ in terms of a piecewise constant Mumford–Shah model. This appears to be well-suited, in particular because the unknown contour is significantly smeared out due to the motion blur. Hence, a comparison of the expected motion blur G_i with the observed time frames g_i in a least square sense $\int_{\Omega} (G_i[\mathcal{O}, w, u_{\text{obj}}, u_{\text{bg}}] - g_i)^2 d\mathcal{L}$ is considered as the fidelity energy, where the length of the boundary contour $\mathcal{H}^1(\mathcal{S})$ acts as the corresponding prior.

For known w and \mathcal{O} , we obtain an almost classical deblurring problem for u_{obj} with the modification of the blurring kernel given in (36), which is already reflected in the above fidelity term. We expect u_{obj} to be characterized by edges (cf. Fig. 17). As a suitable prior for these intensity maps we select the total variation functional $\int_{\Omega} |\nabla u_{\text{obj}}| d\mathcal{L}$ [61], which at the same time guarantees a suitable extension onto the whole space.

Finally, given \mathcal{O} and the two intensities $u_{\text{obj}}, u_{\text{bg}}$, the extraction of the motion velocity w is primarily an optical flow problem. The transport of the object intensity u_{obj} from time t_1 to t_2 described in G_1 and G_2 provides us with information on w . In the case of limited intensity modulations on the moving object, it is the comparison of the expected transition profile $\chi_{\text{obj}} * h_w$, encoded in G_i , with the observed profile in g_i that will act as a guidance for the identification of the motion velocity.

Based on these modeling aspects we finally obtain the energy

$$\mathcal{E}[u_{\text{obj}}, w, \mathcal{S}] = \sum_{i=1,2} \int_{\Omega} (G_i[\mathcal{O}, w, u_{\text{obj}}, u_{\text{bg}}] - g_i)^2 d\mathcal{L} + \mu \int_{\Omega} |\nabla u_{\text{obj}}| d\mathcal{L} + \eta \mathcal{H}^1(\mathcal{S}),$$

and ask for a minimizing set of the degrees of freedom \mathcal{O} , w , and u_{obj} . Once a minimizer is known, we can retrieve the deblurred images $u(t_1, \cdot)$ and $u(t_2, \cdot)$ applying (36). In the application, the joint approach for all three unknowns—the motion velocity w , the object intensity u_{obj} and the shape of the object \mathcal{S} —turns out to be crucial for a proper reconstruction of blurred video frames. This interdependence is demonstrated by the results in Fig. 16 where we compare our joint approach with a two step method which first tries to identify \mathcal{O} and w based on a motion competition algorithm [24], followed by the actual deblurring in a second step. Note that the proposed method can be regarded as a motion competition method if we skip the convolution with the convolution kernel h_w in the variational formulation. Figure 16 also shows the importance of the consistent

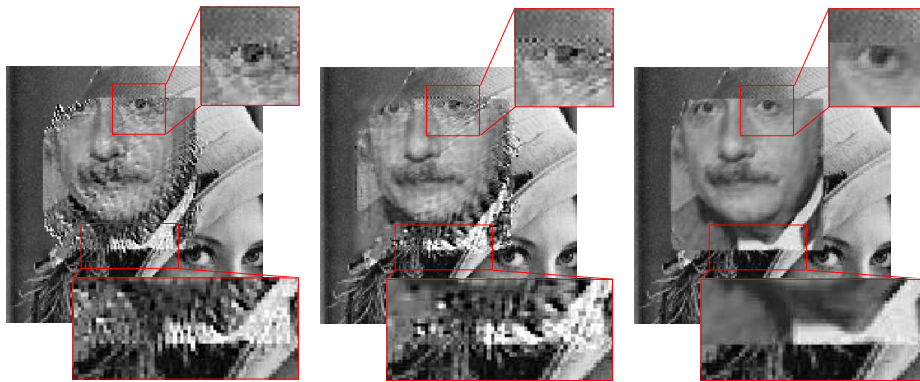


Fig. 16. A comparison of our joint method with a non-joint method and with a method not taking into account the consistent motion blur model is shown. A restored frame with two zoom up areas is depicted for a straightforward scale variant motion deblurring, where the contour is extracted a priori based on pure motion competition (left), for the non-consistent motion blur model on the same a priori computed contour (middle) and for the fully joint method with the consistent model (right).

motion blur model for a proper reconstruction in the vicinity of motion singularities. Finally, we have applied our model to a true motion sequence recorded with a hand held video camera. The sequence shows a toy car moving in front of a puzzle (background) (cf. Fig. 17). We choose a textured object moving in front of a textured background to demonstrate the interplay between the deblurring steered by the fidelity functional and the reconstruction of sharp edges due to the total variation built into the prior. Finally, a real world application is shown in Fig. 17.

4 Elastic shape averaging

This section is concerned with a physically motivated notion of shape averages. As shapes we consider object contours or image morphologies, both encoded as edge sets



Fig. 17. From two real blurred frames (left), we automatically and simultaneously estimate the motion region, the motion vector and the image intensity of the foreground (middle). Based on this and the background intensity we reconstruct the two frames (right)

in images. We again propose to employ concepts from nonlinear elasticity which reflect first principles and to define shape averages which incorporate natural local measures of the underlying deformation and its dissimilarity from an isometry. Furthermore, we will introduce a robust approximation based on a diffusive phase field description of shapes. Averaging is a fundamental task for the quantitative analysis of ensembles of shapes and has already been extensively studied in the literature.

Very basic notions of averaging include the arithmetic mean of landmark positions [23] and the image obtained by the arithmetic mean of the matching deformations [62,9]. For general images there are various qualitatively different notions of averaging. The intension is a fusion or blending to simultaneously represent complementary information of different but related images [45,43]. It appears natural to study relations between shapes or more general image structures via deformations which transform one shape or image onto the another one [23,62,16]. Conceptually, in the last decade correlations of shapes have been studied on the basis of a general framework of a space of shapes and its intrinsic structure. The notion of a shape space was introduced by Kendall [46] already in 1984. Charpiat et al. [15,14] discuss shape averaging and shape statistics based on the notion of the Hausdorff distance of sets. Understanding shape space as an infinite-dimensional Riemannian manifold, Miller et al. [51,52] defined the average \mathcal{S} of samples $\mathcal{S}_i, i = 1, \dots, n$, as the minimizer of

$$\mathcal{E}[\mathcal{S}] = \sum_{i=1}^n d(\mathcal{S}_i, \mathcal{S})^2$$

for some metric $d(\cdot, \cdot)$, e. g. a geodesic distance in the space of shapes. Fuchs et al. [37] proposed a viscoelastic notion of the distance between shapes \mathcal{S} given as boundaries of physical objects \mathcal{O} . The elasticity paradigm for shape analysis on which our approach is founded differs significantly from the metric approach in shape space. Given two shapes \mathcal{S}_1 and \mathcal{S}_2 and an elastic deformation ϕ from \mathcal{S}_1 to \mathcal{S}_2 , we have to distinguish a usually stress free reference configuration \mathcal{S}_1 from the deformed configuration $\mathcal{S}_2 = \phi(\mathcal{S}_1)$, which is under stress and not in equilibrium. Due to the axiom of elasticity the energy at the deformed configuration \mathcal{S}_2 is independent of the path which connects \mathcal{S}_1 with \mathcal{S}_2 . Hence, there is no notion of shortest paths if we consider a purely elastic shape model. As outlined above assumed viscous or visco plastic materials forming a shape, the underlying dissipation allows to measure length of connecting paths as long as the

final configuration is again stress free. Fletcher et al. [35] propose to use a shape median instead of the geometric shape mean. The median is defined as the minimizer of the functional $\mathcal{E}[\mathcal{S}] = \sum_{i=1}^n d(\mathcal{S}_i, \mathcal{S})$.

4.1 A nonlinear elastic spring model

Here, we consider shapes encoded in images. In the simplest case, such an image $u : \Omega \rightarrow \mathbb{R}$ is a characteristic function $u = \chi_{\mathcal{O}}$ representing an object \mathcal{O} as an open set on some domain $\Omega \subset \mathbb{R}^d$ with $d = 2, 3$, and we define the object shape $\mathcal{S} := \partial\mathcal{O}$. More generally we are interested in a shape \mathcal{S} defined as the morphology of an image and represented via the image edge set.

Let us assume that n images $u_i : \Omega \rightarrow \mathbb{R}$ for $i = 1, \dots, n$ are given with a sufficiently regular $(d-1)$ -dimensional edge sets \mathcal{S}_i . We are interested in an average shape which reflects the geometric characteristics of the n given shapes in a physically intuitive manner. Suppose $\mathcal{S} \subset \mathbb{R}^d$ denotes a candidate for this unknown set. Now, we take into account elastic deformations $\phi_i : \Omega \rightarrow \mathbb{R}^d$ with $\phi_i(\mathcal{S}_i) = \mathcal{S}$. Assigned to each of these deformations is an elastic energy $\mathcal{W}[\mathcal{O}_i, \phi_i]$, and we ask for a shape \mathcal{S} such that the total energy given as the sum over all the energies $\mathcal{W}[\mathcal{O}_i, \phi_i]$ for $i = 1, \dots, n$ is minimal. Here, we will again consider a polyconvex elastic energy $\mathcal{W}[\mathcal{O}_i, \phi_i] = \int_{\mathcal{O}_i} \hat{W}(\mathcal{D}\phi) d\mathcal{L}$ given in (8) with the energy density \hat{W} from (9). As described below we will have to consider in addition a further energy contribution which acts as a prior on the shape \mathcal{S} in this variational approach. Obviously, this is a constrained variational problem. We simultaneously have to minimize over n deformations ϕ_i and the unknown shape \mathcal{S} given n constraints $\phi_i(\mathcal{S}_i) = \mathcal{S}$. The model is related to the physical interpretation of the arithmetic mean of n points x_1, \dots, x_n in \mathbb{R}^d . Indeed, the arithmetic mean $x \in \mathbb{R}^d$ minimizes $\sum_{i=1, \dots, n} \alpha d(x, x_i)^2$, where $d(x, x_i)$ is the distance between x and x_i and $\alpha > 0$ is the elasticity constant. Due to Hooke's law the stored energy $\alpha d(x, x_i)^2$ in the spring connecting x_i and x is proportional to the squared distance. Let us restrict the set of admissible deformations for each object \mathcal{O}_i imposing the constraint $\phi_i(\mathcal{S}_i) = \mathcal{S}$ to deduce a suitable energy on shapes \mathcal{S} being candidates for the shape average and sets of deformations $(\phi_i)_{i=1, \dots, n}$ matching given shapes \mathcal{S}_i with \mathcal{S} (cf. 18):

$$\mathcal{E}[\mathcal{S}, (\phi_i)_{i=1, \dots, n}] = \begin{cases} \frac{1}{n} \sum_{i=1, \dots, n} \mathcal{W}[\mathcal{O}_i, \phi_i] & ; \phi_i(\mathcal{S}_i) = \mathcal{S} \text{ for } i = 1, \dots, n \\ \infty & ; \text{else} . \end{cases}$$

Finally, we define the shape average \mathcal{S} as the minimizer over a suitable set of admissible shapes $\mathcal{A}_{\mathcal{S}}$, i. e.

$$\mathcal{S} = \arg \min_{\tilde{\mathcal{S}} \in \mathcal{A}_{\mathcal{S}}} \left(\left(\arg \min_{\phi_i : \mathcal{O}_i \rightarrow \mathbb{R}^d} \mathcal{E}[\tilde{\mathcal{S}}, (\phi_i)_{i=1, \dots, n}] \right) + \eta \mathcal{H}^{d-1}[\tilde{\mathcal{S}}] \right).$$

Here $\eta \mathcal{H}^{d-1}[\tilde{\mathcal{S}}]$ with $\eta > 0$ acts as a prior on admissible shapes. In fact, we interpret the elastic energy $\mathcal{W}[\mathcal{O}_i, \phi_i]$ associated with each deformation ϕ_i which maps one of the shapes \mathcal{S}_i onto the shape \mathcal{S} as a nonlinear counterpart of the energy stored in a spring in the above classical interpretation of an averaged position. It measures in a physically

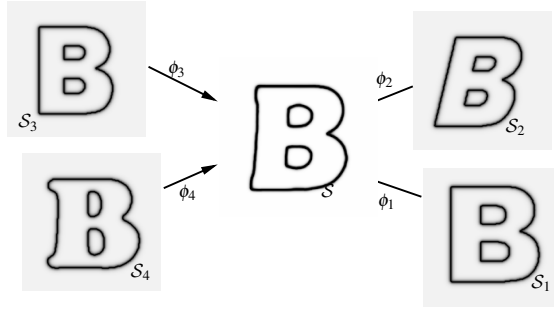


Fig. 18. A sketch of the elastic shape averaging is shown. Input shapes \mathcal{S}_i ($i = 1, \dots, 4$) extracted from input images u_i are mapped onto a shape \mathcal{S} via elastic deformations ϕ_i . The shape \mathcal{S} which minimizes primarily the elastic deformation energy plus some shape prior to be discussed later is called the shape average of the given input shapes. (Displayed are actual numerical results obtained by the algorithm). The resolution of the underlying grid is 257×257 and the values for the involved parameters are $\gamma = 10^7$, $\mu = 1$, $(a_1, a_2, a_3) = (10^6, 0, 10^6)$.

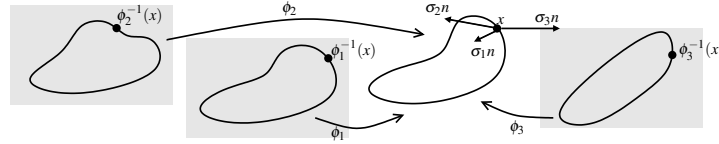


Fig. 19. Sketch of the stress balance relation on the averaged shape. $\sigma_i n$ is short for $\sigma^{\text{def}}[\phi_i]n[\mathcal{S}]$.

rigorous way locally the lack of isometry as already mentioned above (cf. Figure 20). A necessary condition for a set of minimizing deformations are the corresponding Euler Lagrange equations. As usual, inner variations of one of the deformations lead to the classical system of partial differential equations $\text{div } \hat{W}_A(\mathcal{D}\phi_i) = 0$ for every deformation ϕ_i on $\mathcal{O}_i \setminus \mathcal{S}_i$. Due to the set of constraints $(\phi_i(\mathcal{S}_i) = \mathcal{S})_{i=1, \dots, n}$ the conditions on \mathcal{S}_i are interlinked. For simplicity let us assume that $\mathcal{S}_i = \partial\mathcal{O}_i$ for all $i = 1, \dots, n$. Then we can deduce a balance relation between deformation stresses on the averaged shape \mathcal{S} . Namely, for $x \in \mathcal{S}$ we obtain

$$\sum_{i=1, \dots, n} \sigma[\phi_i](\phi_i^{-1}(x))n[\mathcal{S}_i](\phi_i^{-1}(x))\mathcal{H}^{d-1}(\mathcal{S}_i) = 0, \quad (37)$$

where $n[\mathcal{S}_i]$ is the outer normal on \mathcal{S}_i , $\mathcal{H}^{d-1}(\mathcal{S}_i)$ the surface element on \mathcal{S}_i , and $\phi_i^{-1}(x)$ the pre-image of x under the deformation ϕ_i . From elasticity theory we know that the forces $\sigma[\phi_i](\phi_i^{-1}(x))n[\mathcal{S}_i](\phi_i^{-1}(x))\mathcal{H}^{d-1}(\mathcal{S}_i)$ in the reference configuration equal the corresponding forces $\sigma^{\text{def}}[\phi_i](x)n[\mathcal{S}](x)\mathcal{H}^{d-1}[\mathcal{S}]$ in the deformed configuration so that (37) directly implies a balance of all normal stresses on the average shape \mathcal{S} ,

$$0 = \sum_{i=1, \dots, n} \sigma^{\text{def}}[\phi_i](x)n[\mathcal{S}](x),$$

where $n[\mathcal{S}](x)$ is the outer normal in \mathcal{S} and $\sigma^{\text{def}}[\phi_i] \circ \phi_i = \sigma[\phi_i] \det(\mathcal{D}\phi_i)^{-1} \mathcal{D}\phi_i^T$ the usual Cauchy stress tensor corresponding to the deformation ϕ_i in the deformed configuration (cf. Figure 19). This gives a refined physical interpretation of the shape average as the stable shape on which all surface forces implied by the elastic deformations are balanced. Obviously, there is a straightforward generalization involving jumps of normal stresses on interior interfaces in case of components of \mathcal{S}_i which are interior edges in \mathcal{O}_i . The hard constraint $\phi_i(\mathcal{S}_i) = \mathcal{S}$ is often inadequate in applications. Due to local shape fluctuations, for example, or noise in the shape acquisition there are frequently local details like spurious edges in the input shapes which should not be encountered in the shape average. Hence, we relax the constraint and introduce a penalty functional, which measures the symmetric difference of the input shapes \mathcal{S}_i and the pull back $\phi_i^{-1}[\mathcal{S}]$ of the shape \mathcal{S} and is given by

$$\mathcal{F}[\mathcal{S}_i, \phi_i, \mathcal{S}] = \mathcal{H}^{d-1}(\mathcal{S}_i \Delta \phi_i^{-1}[\mathcal{S}]),$$

where $A \Delta B = A \setminus B \cup B \setminus A$. Finally, to sum up, our shape averaging model is based on the energy

$$\mathcal{E}^\gamma[\mathcal{S}, (\phi_i)_{i=1, \dots, n}] = \frac{1}{n} \sum_{i=1}^n \left(\int_{\mathcal{O}_i} \hat{W}(\mathcal{D}\phi_i) d\mathcal{L} + \gamma \mathcal{F}[\mathcal{S}_i, \phi_i, \mathcal{S}] \right) + \eta \mathcal{H}^{d-1}[\mathcal{S}]. \quad (38)$$

This approach is related to groupwise registration and segmentation results [69,70]. Here, \mathcal{F} acts as a fidelity term measuring the quality of the registration of the shapes \mathcal{S}_i with a given shape \mathcal{S} under the deformations ϕ_i . Figure 20 shows results for the averaging of some human figure sketches and underlines that the proposed method measures locally the isometry defect.

4.2 A phase field approximation

As in the registration applications considered so far, we pick up the phase field approximation by Ambrosio and Tortorelli [2,3] and encode the edge set \mathcal{S} by a smooth phase field function $v : \Omega \rightarrow \mathbb{R}$. For the input shapes \mathcal{S}_i we assume the corresponding phase field description v_i to be given a priori. Usually, v_i can be computed beforehand, minimizing the original Ambrosio Tortorelli type energy for given input images u_i , or explicitly constructed for a given edge set using the comparison function from the slicing argument in [3]. Given a phase field parameter ε and corresponding phase field representations v of \mathcal{S} and v_i of \mathcal{S}_i , respectively, we define an approximate mismatch penalty

$$\mathcal{F}^\varepsilon[v_i, \phi_i, v] = \frac{1}{\varepsilon} \int_{\Omega} (v \circ \phi_i)^2 (1 - v_i)^2 + v_i^2 (1 - v \circ \phi_i)^2 d\mathcal{L}.$$

Here, we suppose v to be extended by 1 outside the computational domain Ω . The first term in the integrand is close to 1 on $\mathcal{S}_i \setminus \phi_i^{-1}[\mathcal{S}]$, because $(1 - v_i) \approx 1$ on \mathcal{S}_i and $v \circ \phi_i \approx 1$ away from the vicinity of $\phi_i^{-1}[\mathcal{S}]$. It tends to 0 with increasing distance from this set. Analogously, the second term acts as an approximate indicator function for $\phi_i^{-1}[\mathcal{S}] \setminus \mathcal{S}_i$. Let us emphasize that $\mathcal{F}^\varepsilon[v_i, \phi_i, v]$ is expected to be a true approximation of

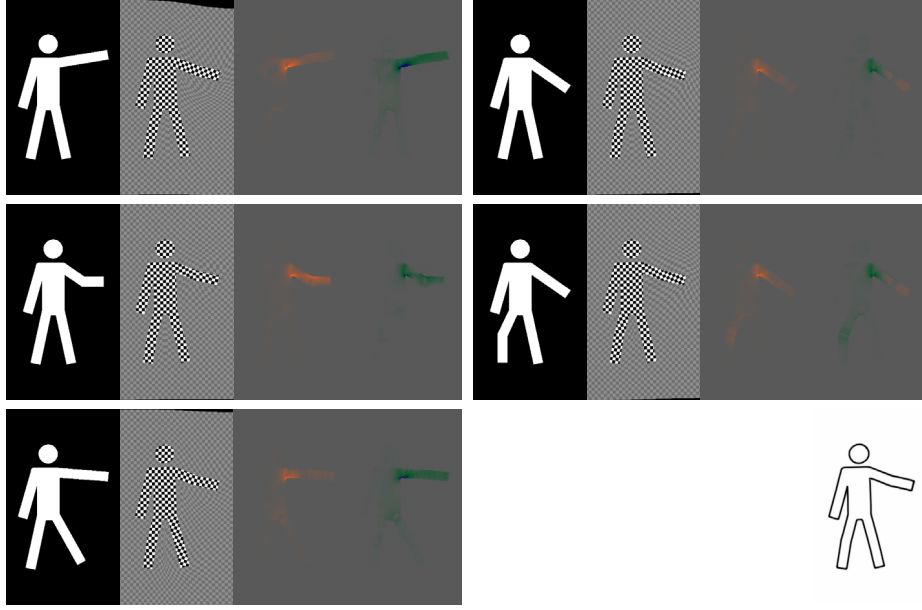


Fig. 20. Given five silhouettes of a person as input shapes a shape average (bottom right) is computed based on our elastic averaging approach. The original images are depicted along with their deformations ϕ_i (continued to the region outside the object and displayed acting on a checkerboard on the image domain Ω) and the distribution of local change of length $|\mathcal{D}\phi_i|_2$ and local change of area $\det(\mathcal{D}\phi_i)$ (from left to right). These local densities ranging over $[0.97, 1.03]$ and $[0.97\sqrt{2}, 1.03\sqrt{2}]$, respectively, are color-coded using the color map . The underlying image resolution is 513×513 , and the energy parameters are $\gamma = 10^7$, $\mu = 10^{-2}$. The phase field parameter in the implementation is chosen equal to the grid size.

$\mathcal{F}[\mathcal{S}_i, \phi_i, \mathcal{S}]$ only, if ϕ_i is neither distending nor compressive orthogonally to the shape, i. e. $\mathcal{D}\phi_i n[\phi_i^{-1}[\mathcal{S}]] \cdot n[\phi_i^{-1}[\mathcal{S}]] = 1$ on $\phi_i^{-1}[\mathcal{S}]$. Nevertheless, because we are primarily interested in the limit for $\gamma \rightarrow \infty$, $\mathcal{F}^\varepsilon[v_i, \phi_i, v]$ acts as a proper penalty functional.

Next, we have to describe the phase field v , which is not given a priori, in an implicit variational form and consider the usual energy

$$\mathcal{H}_\varepsilon^{d-1}[v] = \int_\Omega \varepsilon |\nabla v|^2 + \frac{1}{4\varepsilon} (v-1)^2 d\mathcal{L},$$

which additionally acts as a regularization energy measuring an approximation of the \mathcal{H}^{d-1} measure of the shape \mathcal{S} represented by the phase field v .

So far the elastic energy is evaluated on the object domains \mathcal{O}_i only. For practical reasons of the later numerical discretization, we now let the whole computational domain behave elastically with an elasticity several orders of magnitude softer outside the object domains \mathcal{O}_i on the complement set $\Omega \setminus \mathcal{O}_i$. We suppose that, based on a prior segmentation of the images u_i , a smooth approximation $\chi_{\mathcal{O}_i}^\varepsilon$ of the characteristic function $\chi_{\mathcal{O}_i}$

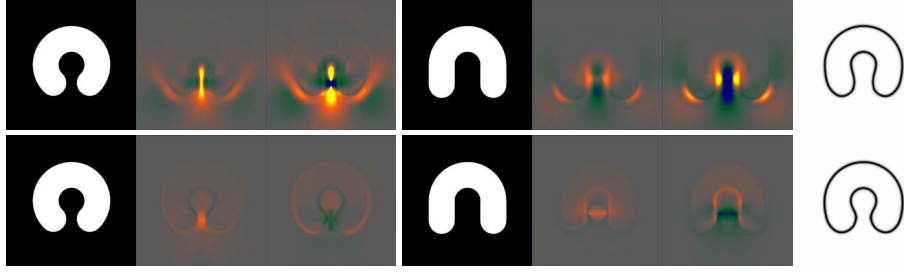



Fig. 21. Input images together with $\|\mathcal{D}\phi_i\|$ and $\det(\mathcal{D}\phi_i)$ (ranges of $[0.6, 1.4]$ and $[0.6\sqrt{2}, 1.4\sqrt{2}]$ color-coded as ) and the average phase field (rightmost). In the top row only the interior of the two shapes behave elastic, whereas in the bottom row the whole computational domain is considered to be homogeneously elastic. Obviously, in the upper case far stronger strains are visible in the region of the gap and in the lower case it is much more expensive to pull the lobes apart in the first shape than to push them together in the second shape. Hence, the resulting average in the second row is characterized by stronger bending of the two lobes similar than in the first row. (Results are obtained for a grid resolution 1025×1025 and parameter values $\gamma = 10^7$, $\mu = 0.1$, $\varepsilon = 6h$.)

is given and define a corresponding approximate elastic energy

$$\mathcal{W}^\varepsilon[\mathcal{O}_i, \phi_i] = \int_{\Omega} \left((1 - \delta) \chi_{\mathcal{O}_i}^\varepsilon + \delta \right) \hat{W}(\mathcal{D}\phi_i) d\mathcal{L},$$

where in our application $\delta = 10^{-4}$. Also, in the above we implicitly assumed that deformations ϕ_i map the domain Ω onto itself; for numerical implementation we will relax this assumption and perform integrations only in regions where all integrands are defined. Finally, the resulting approximation of the total energy functional to be minimized reads

$$\mathcal{E}^{\gamma, \varepsilon}[v, (\phi_i)_{i=1, \dots, n}] = \frac{1}{n} \sum_{i=1}^n (\mathcal{W}^\varepsilon[\mathcal{O}_i, \phi_i] + \gamma \mathcal{F}^\varepsilon[v_i, \phi_i, v]) + \eta \mathcal{H}_\varepsilon^{d-1}[v]. \quad (39)$$

Let us remark that we are particularly interested in the case, where \mathcal{F}^ε acts as a penalty with $\gamma \gg 1$ and $\mathcal{H}_\varepsilon^{d-1}$ ensures a mild regularization of the averaged shape with $\eta \ll 1$. The structure of the penalty functional \mathcal{F}^ε tries to match the shapes of the given phase field functions v_i , and the pull back $v \circ \phi_i$ of the phase field v has to be determined. This implies a particular stiffness of the deformations ϕ_i on the diffused interface around the shapes \mathcal{S}_i . Indeed, there the set of deformations $\phi_1 \dots, \phi_n$ tries to minimize stretch of compression normal to the shape contour measured in terms of $\mathcal{D}\phi \cdot n[\mathcal{S}_i] \cdot n[\mathcal{S}_i] - 1$. In the limit for $\gamma \rightarrow \infty$ this does not hamper the elastic deformation, because the other (tangential) components of the deformation tensor can relax freely. Figure 21 shows the impact of the choice of the elastic domain on the average shape. Here, we once consider the whole computational as homogeneously elastic, and alternatively – and in many cases physically more sound – only the object domain is assumed to be elastic

and considerably stiff. The region between both lobes is more severely dilated if the elastic energy is weighted with a small factor outside the shape, which becomes obvious especially in the plots of the elastic invariants. Furthermore, the particular role of the diffused interface with respect to the compression rates is indicated by the color coding. As first illustrative examples, we computed the average of different 2D objects

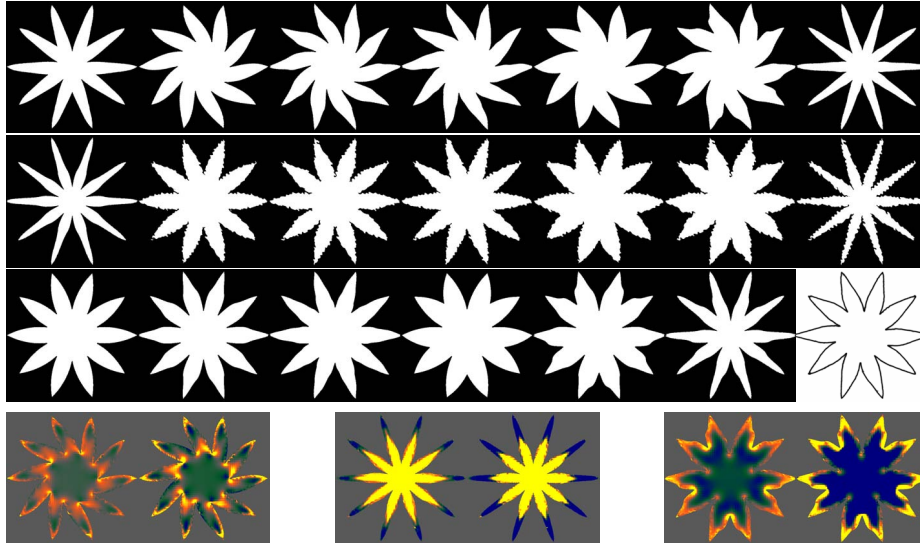



Fig. 22. 20 shapes “device7” from the MPEG7 database and their average phase field. The bottom line shows $|\mathcal{D}\phi_i|_2$ and $\det(\mathcal{D}\phi_i)$ for shape 2, 8, and 18, with ranges of $[0.8, 1.2]$ and $[0.8\sqrt{2}, 1.2\sqrt{2}]$ color-coded as . (Resolution 513×513 , $\gamma = 10^7$, $\mu = 10^{-2}$.)

as shown in Figures 22. Furthermore, Figures 20 has already shown that due to the invariance of the hyperelastic energy with respect to local rotations, the computed averages try to locally preserve isometries. Effectively, the different characteristics of the input shapes, both on the global and a local scale, are averaged in a physically intuitive way, and the scheme proves to perform fairly robust due to the diffusive approximation based on the phase field model and the multi scale relaxation. In what follows we will consider the averaging of 3D shapes originally given as triangulated surfaces and first converted to an implicit representation as binary images. A set of 48 kidneys and a set of 24 feet will serve as input data. We will employ a hyperelastic energy (8) with a density (9) with $p = q = 4$ and $s = r = 2$. The first five original kidneys and their computed average are shown in Figure 23 . In fact, since the average 3D phase field itself cannot be properly displayed, we instead depict one of the original kidneys, deformed to the average configuration. This is allowed, for all deformed kidneys look alike and constitute each just one representative of the average equivalence class in the quotient space of images relative to the edge equivalence relation. (It goes without saying that

the deformed kidney boundaries only coincide up to the width of the phase field.)

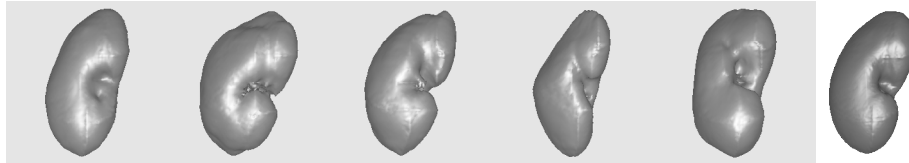


Fig. 23. Five segmented kidneys and their average (right). (Result obtained for resolution $257 \times 257 \times 257$ and parameter values $\gamma = 10^7$, $\mu = 1$, $(a_1, a_2, a_3) = (10^8, 0, 10^7)$.)

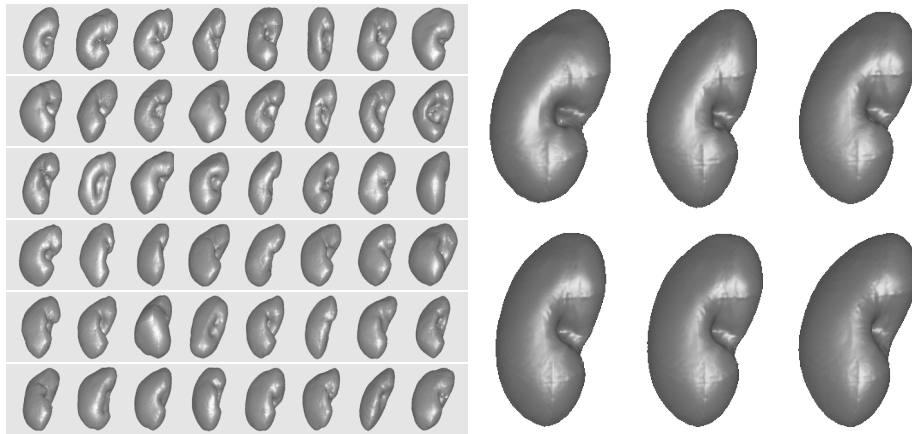


Fig. 24. On the left, 48 kidney shapes are shown. On the right, from top left to bottom down the averaged shape of the first two, four, five, six, eight and of all 48 kidneys are depicted. The parameter values are as for Figure 23.

The next example consists of a set of feet, where the average may help to design an optimal shoe. The 24 original feet are displayed in Figure 25. Their surface is colored according to the local distance to the surface of the computed average shape, which helps to identify regions of strong variation. Furthermore, to allow a better comparison, the foot shapes, have been aligned with the average for the final visualization. Let us emphasize that the algorithm itself robustly deals with even quite large rigid body motions. Apparently, the instep differs comparatively little between the given feet, whereas the toes show a rather strong variation. Note that—since we only display normal distance to the surface of the average foot—any potential tangential displacement is not visible, but could of course also be visualized when examining shape variation.

To illustrate that the approach can also be applied to average image morphologies, let us

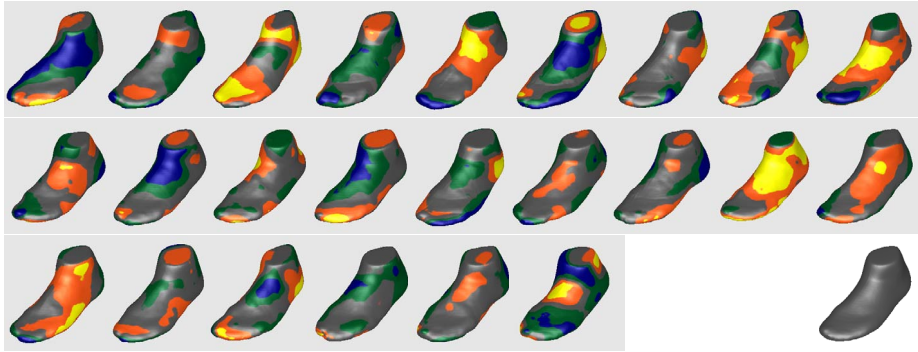


Fig. 25. 24 given foot shapes, textured with the distance to the surface of the average foot (bottom right). Values range from 6 mm inside the average foot to 6 mm outside, color-coded as . For that purpose, the shapes have been aligned to the average. The front of the instep can be identified as a region of comparatively low variation. (Result obtained for resolution 257×257 and parameter values $\gamma = 10^7$, $\mu = 1$, $(a_1, a_2, a_3) = (10^8, 0, 10^8)$.)

consider four two-dimensional, transversal CT scans of the thorax as input (Figure 26, left). Unlike the previous examples, these images do not encode volumetric shapes homeomorphic to the unit ball, but contain far more complicated structures. Also, the quality of contrast differs between the images, and—even more problematic—the images do not show a one-to-one correspondence, i. e. several structures (the scapula, ribs, parts of the liver) are only visible in some images, but not in others. Nevertheless, the algorithm manages to segment and align the main features (the heart, the spine, the aorta, the sternum, the ribs, the back muscles, the skin), yielding sensible average contours (Figure 26, right). In order to achieve this, we this time jointly segmented and averaged the original CT scans, i. e. we augmented our objective function (39) by the original Ambrosio–Tortorelli energy for each image and then alternately optimized for the v_i , v , and ϕ_i . The second to fourth column of Figure 26 depict the corresponding deformations ϕ_i and the deformation invariants. Obviously, the deformation behaves quite regularly: Not only is it homeomorphic, but also too large and distorting deformations are prevented by the hyperelastic regularization. This enables the method to be applied to images containing also distinct structures, whereas for viscous flow regularization as in [11,17] such individual structures are at risk of being matched with anything nearby (a frequently used example for viscous fluid regularization even matches a disc to a C-shape). The deformation energy is quite evenly distributed over the images and only peaks at pronounced features, where a local exact fit can be achieved (e. g. at the back muscles). Outside the thorax, the energy rapidly decreases to zero, justifying that in this example we did not weight the elastic energy differently inside and outside the body.

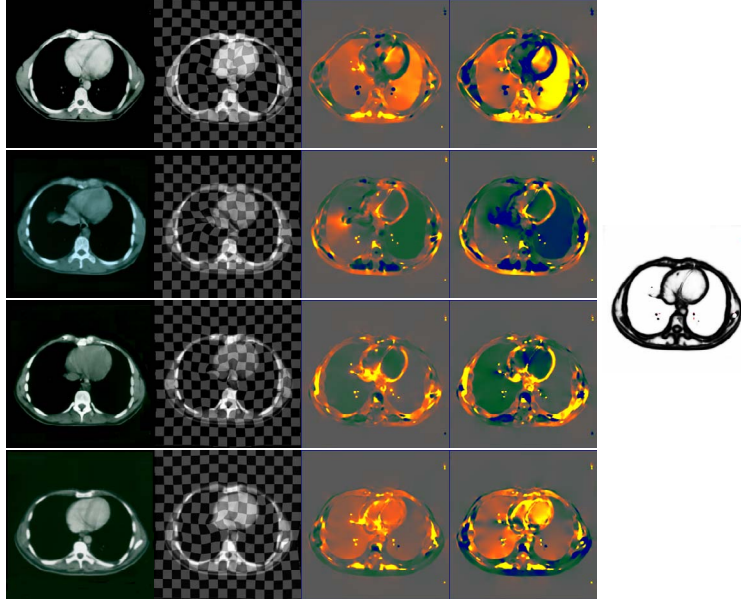



Fig. 26. Averaging of four CT scans of the thorax. From left to right: Original images, deformations ϕ_i , $|\mathcal{D}\phi_i|_2$ and $\det(\mathcal{D}\phi_i)$ (color-coded as  with ranges $[0.8, 1.2]$ and $[0.8\sqrt{2}, 1.2\sqrt{2}]$), and average phase field. (Result obtained for resolution 257×257 and parameter values $\gamma = 10^7$, $\mu = 0.1$.)

4.3 Joint image segmentation and shape averaging

In the derivation of our shape averaging model we have assumed that the shapes \mathcal{S}_i to be averaged can be robustly extracted from a set of images u_i with $i = 1, \dots, n$ and are a priori given. However, if we consider shapes being defined as the morphology of images represented by edges, some of these edges will be characterized by significant noise or low contrast and hence will be difficult to extract. Here, it might help to take into account the corresponding edges in the other images, which all refer to the same edge of the average shape. Indeed, in this case a joint approach of shape segmentation and registration with an averaged shape is particularly promising: On the one hand the quality of shape averaging highly depends on the robustness of the edge detection in the input images. On the other hand, a reliable average shape can be used to improve edge detection in case of a poor image quality. Incorporating the classical Mumford Shah segmentation approach in the above shape averaging functional (38) we end up with the joint functional

$$\begin{aligned} \mathcal{E}_{\text{joint}}^\gamma[\mathcal{S}, (u_i, \mathcal{S}_i, \phi_i)_{i=1, \dots, n}] &= \frac{1}{n} \sum_{i=1}^n (\mathcal{E}_{\text{MS}}[u_i, \mathcal{S}_i] + \mathcal{W}[\Omega, \phi_i] + \gamma \mathcal{F}[\mathcal{S}_i, \phi_i, \mathcal{S}]) \\ &\quad + \mu \mathcal{H}^{d-1}[\mathcal{S}], \end{aligned}$$

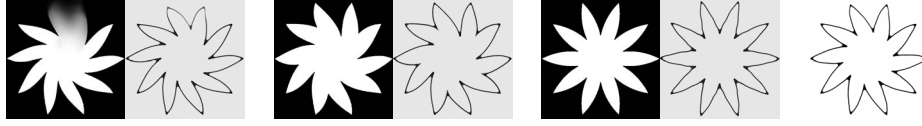


Fig. 27. Blurred edges can be restored based on a joint approach for image segmentation and averaging. The three input images u_i^0 are depicted along with their phase field v_i as computed by the joint segmentation and averaging. The computed average shape is also shown (right). Apparently, the strongly blurred edges in the first input image were reconstructed based on the corresponding edges in the other images. (Resolution 513×513 , $\gamma = 10^7$, $\mu = 10^{-2}$, $(a_1, a_2, a_3) = (10^8, 0, 10^8)$, $\alpha = 2 \cdot 10^{10}$, $\beta = 2 \cdot 10^5$, $\eta = 2 \cdot 10^6$.)

which has to be relaxed simultaneously in u_i , \mathcal{S}_i , ϕ_i for $i = 1, \dots, n$ and \mathcal{S} for a given set of input images $(u_i^0)_{i=1, \dots, n}$. Let us remark that we use the parameter μ for the weighting of the area of the shape \mathcal{S} , because an η already weight the area of the input shape \mathcal{S}_i . Finally, let us consider the phase field approximation for this joint model given by the functional

$$\mathcal{E}_{\text{joint}}^{\gamma, \varepsilon}[v, (u_i, v_i, \phi_i)_{i=1, \dots, n}] = \frac{1}{n} \sum_{i=1}^n (\mathcal{E}_{\text{AT}}^{\varepsilon}[u_i, v_i] + \mathcal{W}^{\varepsilon}[\mathcal{O}_i, \phi_i] + \gamma \mathcal{F}^{\varepsilon}[v_i, \phi_i, v_i]) + \mu \mathcal{H}_{\varepsilon}^{d-1}(v).$$

where $\mathcal{E}_{\text{AT}}^{\varepsilon}[u_i, v_i]$ denotes the classical Ambrosio Tortorelli functional for given image intensities u_i^0 and for $i = 1, \dots, n$. Figure 27 demonstrates that in a joint approach blurry edges in the input images can be segmented, if sufficiently strong evidence for this edge from other input images is integrated into the averaged shape.

Acknowledgment

The author is grateful to Werner Bautz, radiology department at the university hospital Erlangen, Germany, for providing CT data of kidneys, as well as to Heiko Schlarb from Adidas, Herzogenaurach, Germany, for providing 3D scans of feet, and to Bruno Wirth, urology department at the Hospital zum Hl. Geist, Kempen, Germany, for providing thorax CT scans. Furthermore, the author thanks Stan Osher for pointing to the issue of elastic shape averaging and Marc Droske for discussion about the phase field approach. Finally, he acknowledges Helene Horn for her help in the careful preparation of the manuscript.

References

1. Luis Alvarez, Frédéric Guichard, Pierre-Louis Lions, and Jean-Michel Morel. Axioms and fundamental equations of image processing. *Arch. Ration. Mech. Anal.*, 123(3):199–257, 1993.

2. L. Ambrosio and V. M. Tortorelli. Approximation of functionals depending on jumps by elliptic functionals via Γ -convergence. *Comm. Pure Appl. Math.*, 43:999–1036, 1990.
3. L. Ambrosio and V. M. Tortorelli. On the approximation of free discontinuity problems. *Bollettino dell'Unione Matematica Italiana, Sezione B*, 6(7):105–123, 1992.
4. Luigi Ambrosio, Nicola Fusco, and Diego Pallara. *Functions of bounded variation and free discontinuity problems*. Oxford Mathematical Monographs. Oxford University Press, New York, 2000.
5. T.J. Baker. Three dimensional mesh generation by triangulation of arbitrary point sets. In *Computational Fluid Dynamics Conference, 8th, Honolulu, HI, June9-11, 1987*, volume 1124-CP, pages 255–271, 1987.
6. J. M. Ball. Convexity conditions and existence theorems in nonlinear elasticity. *Archive of Rational Mechanics and Analysis*, 63:337–403, 1977.
7. J.M. Ball. Global invertibility of Sobolev functions and the interpenetration of matter. *Proc. Roy. Soc. Edinburgh*, 88A:315–328, 1988.
8. L. Bar, B. Berkels, M. Rumpf, and G. Sapiro. A variational framework for simultaneous motion estimation and restoration of motion-blurred video. In *Eleventh IEEE International Conference on Computer Vision (ICCV'07)*, 2007.
9. K. K. Bhatia, J. V. Hajnal, B. K. Puri, A. D. Edwards, and D. Rueckert. Consistent groupwise non-rigid registration for atlas construction. In *IEEE International Symposium on Biomedical Imaging: Nano to Macro*, volume 1, pages 908–911, 2004.
10. B. Bourdin. Image segmentation with a Finite Element method. Technical Report Report Nr. 00-14, Institut Galilée Université Paris Nord, UCLA CAM, 2000. article: *Math. Model. Numer. Anal.*, Vol. 33, No. 2, pp. 229–244, 1999.
11. M. Bro-Nielsen and C. Gramkow. Fast fluid registration of medical images. In K. H. Höhne and R. Kikinis, editors, *Visualization in Biomedical Computing: 4th International Conference, VBC*, volume 1131 of *LNCS*, pages 267–276, 1996.
12. L.G. Brown. A survey of image registration techniques. *ACM Computing Surveys*, 24(4):325–376, 1992.
13. T. Chan and L. Vese. An active contour model without edges. In M. Nielsen, P. Johansen, O. F. Olsen, and J. Weickert, editors, *Scale-Space Theories in Computer Vision. Second International Conference, Scale-Space '99, Corfu, Greece, September 1999*, Lecture Notes in Computer Science; 1682, pages 141–151. Springer, 1999.
14. G. Charpiat, O. Faugeras, R. Keriven, and P. Maurel. Distance-based shape statistics. In *Acoustics, Speech and Signal Processing, 2006 (ICASSP 2006)*, volume 5, 2006.
15. Guillaume Charpiat, Olivier Faugeras, and Renaud Keriven. Approximations of shape metrics and application to shape warping and empirical shape statistics. *Foundations of Computational Mathematics*, 5(1):1–58, 2005.
16. G. E. Christensen, S. C. Joshi, and M. I. Miller. Volumetric transformations of brain anatomy. *IEEE Trans. Medical Imaging*, 16, no. 6:864–877, 1997.
17. G. E. Christensen, R. D. Rabbitt, and M. I. Miller. A deformable neuroanatomy textbook based on viscous fluid mechanics. In J. Prince and T. Runolfsson, editors, *Proc. 27th Annual Conf. Information Sci. and Systems*, pages 211–216, 1993.
18. G.E. Christensen, M.I. Miller, and R.D. Rabbitt. Deformable templates using large deformation kinematics. *IEEE Trans. Image Processing*, 5(10):1435–1447, 1996.
19. P. G. Ciarlet. *Three-dimensional elasticity*. Elsevier Science Publishers B. V., 1988.
20. Philippe G. Ciarlet and Jindřich Nečas. Injectivity and self-contact in nonlinear elasticity. *Arch. Rational Mech. Anal.*, 97(3):171–188, 1987.
21. U. Clarenz, M. Droske, and M. Rumpf. Towards fast non-rigid registration. In *Inverse Problems, Image Analysis and Medical Imaging, AMS Special Session Interaction of Inverse Problems and Image Analysis*, volume 313, pages 67–84. AMS, 2002.

22. U. Clarenz, N. Litke, and M. Rumpf. Axioms and variational problems in surface parameterization. *Computer Aided Geometric Design*, 21 (8):727 – 749, 2004.
23. T. F. Cootes, C. J. Taylor, D. H. Cooper, and J. Graham. Active shape models—their training and application. *Computer Vision and Image Understanding*, 61(1):38–59, 1995.
24. D. Cremers and S. Soatto. Motion competition: A variational approach to piecewise parametric motion segmentation. *The International Journal of Computer Vision*, 2004.
25. B. Dacorogna. *Direct methods in the calculus of variations*. Springer-Verlag, New York, 1989.
26. C. A. Davatzikos, R. N. Bryan, and J. L. Prince. Image registration based on boundary mapping. *IEEE Trans. Medical Imaging*, 15(1):112–115, 1996.
27. M. C. Delfour and J.P. Zolésio. *Geometries and Shapes: Analysis, Differential Calculus and Optimization*. Adv. Des. Control 4. SIAM, Philadelphia, 2001.
28. M. Droske and W. Ring. A Mumford-Shah level-set approach for geometric image registration. *SIAM Appl. Math.*, 2008. to appear.
29. M. Droske and M. Rumpf. A variational approach to non-rigid morphological registration. *SIAM Appl. Math.*, 64(2):668–687, 2004.
30. M. Droske and M. Rumpf. Multi scale joint segmentation and registration of image morphology. *IEEE Transaction on Pattern Recognition and Machine Intelligence*, 29(12):2181–2194, 2007.
31. Marc Droske, Wolfgang Ring, and Martin Rumpf. Mumford-Shah based registration: a comparison of a level set and a phase field approach. *Computing and Visualization in Science*, Online First, 2008.
32. Mathieu Desbrun Peter Schröder Eitan Grinspun, Anil N. Hirani. Discrete shells. In *Eurographics/SIGGRAPH Symposium on Computer Animation*, 2003.
33. Paolo Favaro and Stefano Soatto. A variational approach to scene reconstruction and image segmentation from motion-blur cues. In *2004 IEEE Computer Society Conference on Computer Vision and Pattern Recognition (CVPR'04) - Volume 1*, pages 631–637, 2004.
34. O. Féron and A. Mohammad-Djafari. Image fusion and unsupervised joint segmentation using a HMM and MCMC algorithms. *J. of Electronic Imaging*, 2004. to appear.
35. Tom Fletcher, Suresh Venkatasubramanian, and Sarang Joshi. Robust statistics on riemannian manifolds via the geometric median. In *IEEE Conference on Computer Vision and Pattern Recognition (CVPR)*, 2008.
36. I. Fonseca and S. Müller. Quasi-convex integrands and lower semicontinuity in L^1 . *SIAM J. Math. Anal.*, 23, Issue 5:1081–1098, 1992.
37. M. Fuchs, B. Jüttler, O. Scherzer, and H. Yang. Shape metrics based on elastic deformations. Forschungsschwerpunkt S92, Industrial Geometry 71, Universität Innsbruck, 2008.
38. Xianfeng Gu and Baba C. Vemuri. Matching 3D shapes using 2D conformal representations. In *MICCAI 2004*, LNCS 3216, pages 771–780, 2004.
39. W. Hackbusch and S. A. Sauter. Composite finite elements for problems containing small geometric details. Part II: Implementation and numerical results. *Computing and Visualization in Science*, 1(1):15–25, 1997.
40. W. Hackbusch and S. A. Sauter. Composite finite elements for the approximation of PDEs on domains with complicated micro-structures. *Numerische Mathematik*, 75:447–472, 1997.
41. Wolfgang Hackbusch. *Iterative Solution of Large Sparse Systems of Equations*, volume 95 of *Applied Mathematical Sciences*. Springer, 1994.
42. M. Hintermüller and W. Ring. An inexact newton-cg-type active contour approach for the minimization of the mumford-shah functional. *Journal of Mathematical Imaging and Vision*, 20(1-2):19–42, 2004.
43. S. Joshi, B. Davis, M. Jomier, and G. Gerig. Unbiased diffeomorphic atlas construction for computational anatomy. *NeuroImage*, 23:S151–S160, 2004. Supplement 1.

44. T. Kapur, L. Yezzi, and L. Zöllei. A variational framework for joint segmentation and registration. *IEEE CVPR - MMBIA*, pages 44–51, 2001.
45. S. L. Keeling and W. Ring. Medical image registration and interpolation by optical flow with maximal rigidity. *Journal of Mathematical Imaging and Vision*, 23 (1):47–65, 2005. to appear.
46. D. G. Kendall. Shape manifolds, procrustean metrics, and complex projective spaces. *Bull. London Math. Soc.*, 16:81–121, 1984.
47. Vladislav Kraevoy and Alla Sheffer. Cross-parameterization and compatible remeshing of 3D models. *ACM Transactions on Graphics*, 23(3):861–869, August 2004.
48. Aaron Lee, David Dobkin, Wim Sweldens, and Peter Schröder. Multiresolution mesh morphing. In *Proceedings of SIGGRAPH 99*, Computer Graphics Proceedings, Annual Conference Series, pages 343–350, August 1999.
49. N. Litke, M. Droske, M. Rumpf, and P. Schröder. An image processing approach to surface matching. In M. Desbrun and H. Pottmann, editors, *Third Eurographics Symposium on Geometry Processing*, pages 207–216, 2005.
50. J. E. Marsden and T. J. R. Hughes. *Mathematical foundations of Elasticity*. Prentice–Hall, Englewood Cliffs, 1983.
51. M. I. Miller and L. Younes. Group actions, homeomorphisms and matching: a general framework. *International Journal of Computer Vision*, 41(1-2):61–84, 2001.
52. M.I. Miller, A. Trounev, and L. Younes. On the metrics and euler-lagrange equations of computational anatomy. *Annual Review of Biomedical Engineering*, 4:375–405, 2002.
53. J.M. Morel and S. Solimini. *Variational models in image segmentation*. Birkäuser, 1994.
54. Ch. Morrey. Quasi-convexity and lower semicontinuity of multiple integrals. *Pac. J. Math.*, 2:25–53, 1952.
55. Ch. Morrey. *Multiple Integrals in the Calculus of Variations*. Grundlehren Math. Wissen Vol.130 Springer–Verlag, New-York, 1966.
56. D. Mumford and J. Shah. Optimal approximation by piecewise smooth functions and associated variational problems. *Communications on Pure Applied Mathematics*, 42:577–685, 1989.
57. R. W. Ogden. *Non-Linear Elastic Deformations*. John Wiley, 1984.
58. S. J. Osher and N. Paragios. *Geometric Level Set Methods in Imaging, Vision and Graphics*. Springer, 2003.
59. S. J. Osher and J. A. Sethian. Fronts propagating with curvature dependent speed: Algorithms based on Hamilton–Jacobi formulations. *Journal of Computational Physics*, 79:12–49, 1988.
60. Emil Praun, Wim Sweldens, and Peter Schröder. Consistent mesh parameterizations. In *Proceedings of ACM SIGGRAPH 2001*, Computer Graphics Proceedings, Annual Conference Series, pages 179–184, August 2001.
61. L. Rudin, S. Osher, and E. Fatemi. Nonlinear total variation based noise removal algorithms. *Physica D*, 60:259–268, 1992.
62. D. Rueckert, A. F. Frangi, and J. A. Schnabel. Automatic construction of 3D statistical deformation models using nonrigid registration. In W. Niessen and M. Viergever, editors, *Medical Image Computing and Computer–Assisted Intervention, MICCAI*, volume 2208 of *LNCIS*, pages 77–84, 2001.
63. Martin Rumpf and Benedikt Wirth. A nonlinear elastic shape averaging approach. *Submitted to SIAM Journal on Imaging Sciences*, 2008.
64. G. Sapiro. *Geometric Partial Differential Equations and Image Analysis*. Cambridge University Press, 2001.
65. John Schreiner, Arul Asirvatham, Emil Praun, and Hugues Hoppe. Inter-surface mapping. *ACM Transactions on Graphics*, 23(3):870–877, August 2004.
66. J. Sokołowski and J-P. Zolésio. *Introduction to shape optimization*. Springer-Verlag, Berlin, 1992. Shape sensitivity analysis.

67. P. A. van den Elsen, E.-J. J. Pol, and M. A. Viergever. Medical image matching: A review with classification. *IEEE Engineering in Medicine and Biology*, 12:26–39, 1993.
68. V. Šverák. Regularity properties of deformations with finite energy. *Arch. Rat. Mech. Anal.*, 100:105–127, 1988.
69. P. P. Wyatt and J. A. Noble. MAP MRF joint segmentation and registration. In T. Dohi and R. Kikinis, editors, *MICCAI*, volume 2488 of *LNCS*, pages 580–587, 2002.
70. A. Yezzi, L. Zöllei, and T. Kapur. A variational framework for integrating segmentation and registration through active contours. *Medical Image Analysis*, 7(2):171–185, 2003.
71. Yuan-Nan Young and Doron Levy. Registration-based morphing of active contours for segmentation of ct scans. *Mathematical biosciences and Engineering*, Volume 2, Number 1, :79–96, 2005.